INTERNATIONAL JOURNAL FOR NUMERICAL METHODS IN FLUIDS, VOL. 25, 315–366 (1997)

UNSTEADY TWO-DIMENSIONAL TURBULENT VISCOUS FLOW PAST AEROFOILS

E. GUILMINEAU, J. PIQUET* AND P. QUEUTEY

CFD Group, LMF-URA1217 CNRS, ECN, 1 Rue de la Noe, F-44072 Nantes Cedex, France

SUMMARY

The so-called CPI finite volume method is applied to the computation of the deep dynamic stall of a pitching NACA 0012 aerofoil. The evolution of flow sequences is analysed for two turbulence models, the so-called Baldwin–Barth and K–ω SST models, and compared with available data of McAlister *et al.* The hysteresis loops for the force coefficients are presented for three different reduced frequencies of the pitching motion and compared with experimental data. The agreement with available data is good during the upstroke phase and it is found that the level of disagreement during the downstroke phase can be attributed to the overestimation of the pressure minima within shed vortices. © 1997 by John Wiley & Sons, Ltd.

Int. J. Numer. Meth. Fluids, **25**: 315–366 (1997)

No. of Figures: 10. No. of Tables: 2. No. of References: 40.

KEY WORDS: viscous flow; dynamic stall; turbulent flow; aerofoils

1. INTRODUCTION

Accurate estimation of forces and moments acting on an aerofoil at high incidence is an important part of the wing design process. The difficulties associated with viscous flow computations inhibit their routine use in engineering calculations. Difficulties are both numerical (accuracy and grid independence of viscous flow predictions) and physical (turbulence modelling, transition, scale effects). Moreover, the validation of two-dimensional calculations using available experimental data is difficult because such data are often contaminated by tunnel wall or end-plate interference effects. Physical difficulties are particularly noteworthy in stall and post-stall situations where the flow involves massive separation and unsteady phenomena. This makes the accurate prediction of stall incidence and maximum lift coefficient as required by manufacturers particularly challenging. Past stall the flow field structure (vortex shedding) and the unsteady forces are important factors in dynamic stability and control studies, particularly for military fighter applications where low-speed, high-incidence flight is desirable. Another important area involving significant regions of separated flows is in applications using propeller or helicopter rotor blades.

The present work deals with the complex problem of dynamic stall: the incidence is taken as a sinusoidal function of time so that the aerofoil is submitted to a pitching motion around an incidence close to that corresponding to $\alpha_{\max}$, the fixed (static stall) incidence above which the lift of the aerofoil would drop. Dynamic stall differs from its static counterpart in two major ways. First, the

---

* Correspondence to: J. Piquet, CFD Group, LMF-URA1217 CNRS, ECN, 1 Rue de la Noe, F-44072 Nantes Cedex, France

CCC 0271–2091/97/030315–52 $17.50

Received April 1996

maximum lift obtainable under dynamic conditions is greater than that under static conditions. Secondly, while static lift is uniquely related to incidence, stall depends upon the time history of motion and has a hysteresis loop associated with it. This time history makes dynamic stall predictions particularly difficult, especially for deep stall cases in which the oscillation amplitude around the mean angle of incidence α_0 is of the order of α_0, while α_0 is close enough to $\alpha_{\max}$.

A lot of phenomena are known to influence stall characteristics such as drag, lift and moment coefficients. Although the different values of C_{Lmax} for $M < 0{\cdot}4$ are caused by Reynolds number variations, while compressibility effects are negligible, the peak velocity on the aerofoil at stall angles of attack is several times higher than at zero incidence, indicating that the assumption of incompressible flow may be incorrect for velocity fields. For this reason we use only very-low-Mach-number data in order to minimize compressibility effects.

Despite these difficulties, computational studies have addressed the stall problem for a long time. In the following we summarize the available turbulent flow simulations which have been performed for angles of incidence which vary in a sinusoidal way (Tables I and II). Although instructive, laminar flow calculations of a dynamic stall loop have not been considered. The tables gather the following information. In Table I left to right we give the author(s), the first published references of the method,[1–19] the turbulence model used, the wall region treatment, the method of grid generation, the main characteristics of the method used for the momentum equations and the algebraic solution of the resulting discrete problem. Table II gives the author(s) of the described method, the space and time discretizations, the grid size and its topology (C, H or O), the size of the computational domain, the location of the first grid line away from the wall and the test conditions: Reynolds number, Mach number and incidence as well as the reduced frequency of oscillation $k = 2\pi f U_\infty / 2c$ and (in parentheses) the location around which the aerofoil is pitched; finally some comments on the tests are given.

The available methods can be seen to belong to two distinct categories. Most of the methods use the incompressible flow equations with either a collocative approach (as in the present method) or a staggered grid approach. The pressure–velocity coupling is treated in an iterative way using standard segregation techniques[20] such as PISO or SIMPLER, or a penalty approach, or a pseudocompressibility algorithm. The other methods starts from the compressible flow equations and use either the so-called Briley–MacDonald approach with an ADI method following the pioneering efforts of Shamroth and Gibeling,[2,3] or the thin layer Navier–Stokes approximation with an approximate factorization of Beam and Warming type.[21] While the former method seems particularly adequate for low Mach numbers, the latter has been developed with the purpose of addressing more specifically transonic flows with adequate shock-capturing techniques.

While the time discretization is most often the (second-order) fully implicit backward Euler type (except for Reference 19 which uses a Runge–Kutta explicit method), incompressible flow methods in general use hybrid schemes for the numerical treatment of convective terms. Second-order accuracy is a required condition for a good description of dynamic stall cases, since the time integration has to be carried out over at least two periods of oscillations. Compressible flow methods in general use space-centred second-order schemes with systematic explicit fourth-order dissipation and, eventually, second-order implicit dissipation. Flux vector splitting with upwind-type schemes is also encountered[6,10] and this avoids the need for artificial dissipation.

Significant differences are noticeable with regard to turbulence modelling. The so-called algebraic eddy viscosity models are the most used, generally the Baldwin–Lomax (BL) model.[22] This is of course due to its technical simplicity. Other choices include one-equation models such as the K–l model in which the length scale l has to be algebraically satisfied,[2,3] or the so-called Baldwin–Barth (BB) model[23] which solves an additional equation for the eddy viscosity.[17] There is, however, a significant trend towards the use of two-equation models, for the main reason that they produce the

Table I

Author(s)	Reference	Turbulence	Wall region	Grid generation	Momentum equation	Solver
Chyu *et al.*[1]	AIAA 79-1554	BL	No	Elliptic	TLNS-AF Beam–Warming	Pentadiagonal solver
Shamroth and Gibeling[2,3]	AGARD CP 296	K–l Fish–Macdonald	No	Analytic	Collocated grid Briley–McDonald	Block elimination ADI Douglas–Gunn
Tassa and Sankar[4,5]	AIAA 81-1289	BL	No	Elliptic	Briley–McDonald	ADI Douglas–Gunn
Hegna[6]	AIAA 82- 0092	Cebeci–Smith	No	Elliptic	Collocated grid	Chorin, SOR
Rumsey and Anderson[7]	AIAA 88-0329	BL, JK	No	Elliptic	TLNS-AF	Block tridiagonal solver
Visbal[8–10]	AIAA 88-0132	BL	No	Elliptic	TLNS- AF	
Tuncer *et al.*[11]	AIAA 89- 0021	BL	No	Conformal	W eq. + Biot–Savart	Fourier series + SOR
Wu *et al.*[12]	AIAA 89-0609	BL, JK, K–ε	Gorski (K– ε)	Conformal	AF Beam–Warming	Pentadiagonal solver
Dindar and Kaynak[13]	AIAA 92-0027	BL, JK	No	Hyperbolic	AF with LU-ADI	Pulliam–Chaussee
Rizzetta and Visbal[14]	AIAA J., 1993	BL, K–ε	No	Conformal	AF Beam–Warming	Pentadiagonal solver
Srinivasan *et al.*[15]	AIAA 93-3403	5 models	No	Elliptic	AF Beam–Warming	Pentadiagonal solver
Ekaterinaris[16]	AIAA 89-0024	BL	No	Elliptic	Briley–McDonald	ADI Douglas–Gunn
Ekaterinaris and Menter[17]	AIAA J., 1994	K–ω, BB, SA	No	Elliptic	Steger–Warming	Approx. factorization
Yang[18]	AIAA 94- 0286	BL, K–ε	WF with K– ε		Collocated grid	Pressure correction
Niu *et al.*[19]	AIAA 94- 0308	?	No (?)	Elliptic	Steger–Warming modif.	?

Key: WF: wall functions.

Table II.

Author(s)	Space δ	Time δ	Grid	Domain	Resolution	Test case(s)	$10^{-6}Re$	Ma	α (°)	k	(axis)	Remarks
Chyu *et al.*[1]	Steger $O(h^2)$	Euler $O(\Delta t^2)$	87 × 41 C	8c	?	NACA 64A010	2·5–12·5	0·5–0·8	0 ± 1	0·2	($c/4$)	Phase analysis
Shamroth and Gibeling[2,3]	Ctrd. h^2 + diss. h^4	Euler bwd.	81 × 39 C		$2 \times 10^{-5}c$	NACA 0012	1	0·147	6 ± 13	0·1	($c/2$)	Massive stall
Tassa and Sankar[4,5]	$O(h^2)$ + 4th art. damping	Euler $O(\Delta t^2)$	49 × 31	16c	$10^{-4}c$	NACA 0012	2·5	0·3	15 ± 5	0·15–0·5	($c/2$)	Coarse grid
						ONERA Cambré	2·5	0·3	15 ± 5	0·25	($c/2$)	
Hegna[6]	Hybrid	Euler $O(\Delta t)$	83 × 44 O	?	$y^+ = 5$	NACA 0012	0·17	0	3 ± 5	0·41	($c/2$)	C_p, lift and drag
Rumsey and Anderson[7]	Roe + limiter	Euler $O(\Delta t)$	257 × 97 C	15c	$2{\cdot}15 \times 10^{-6}c$	NACA 0012	4·8	0·6	$4{\cdot}86 \pm 2{\cdot}44$	0·162		
Visbal[8–10]	Ctrd. + diss. h^2–h^4	Euler $O(\Delta t^2)$	O	30c	$10^{-5}c$	NACA 0015	2–3	0·2–0·6		0·12–1·26	($c/4$)	Const. pitch-up
Tuncer *et al.*[11]	$O(h^2)$ upwd.	Euler $O(\Delta t)$	80 × 60 O			Joukowski	1	0	$5 \pm 12{\cdot}5$	1–0·25	($c/4$)	Correct loops
Wu *et al.*[12]	Cntrd. + diss. h^2–h^4	Euler $O(\Delta t)$				NACA 0012	3·45	0·28	15 ± 10	0·151		
Dindar and Kaynak[13]	Cntrd. + diss. h^2–h^4	Euler $O(\Delta t^2)$	215 × 60 C	20c	$10^{-5}c$	NACA 0012	4	0·3	10 ± 10	0·1		+ Light stall cases
Rizzetta and Visbal[14]	Cntrd. + diss. h^2–h^4	Euler $O(\Delta t^2)$	303 × 131 C			SSC-A09	2, 4	0·2–0·4		0·02–0·2		Const. pitch-up
Srinivasan *et al.*[15]	$O(h^2)$ + 4th art. damping	Euler $O(\Delta t^2)$	671 × 71 C 361 × 141 C	15c	$2 \times 10^{-5}c$	NACA 0015	1·95	0·294	$15 \pm 4{\cdot}2$	0·1		
Ekaterinaris[16]	$O(h^2)$ + 4th art. damping	Euler $O(\Delta t^2)$	201 × 58 C	8c		SSC-A09	2	0·2	15 ± 5	0·1	($c/2$)	Compress. effects
Ekaterinaris and Menter[17]	Osher + Steger–Warming	Euler $O(\Delta t)$	311 × 91 C	?	$10^{-5}c$, $y^+ = 2$	NACA 0015	2	0·34	$15 \pm 4{\cdot}2$	0·1		Grid refinement
			421 × 151			NACA 0012	4	0·3	10 ± 5	0·1		Transition effects
Yang[18]	TVD $O(h^3)$	Euler $O(\Delta t^2)$	200 × 1000		$y^+ = 0{\cdot}2$, 14 (WF)	NACA 0015	1·95	0·29	$4 \pm 4{\cdot}2$	0·05		+ Constant pitch
						NACA 0012	3·7	0·283	15 ± 10	0·15		detailed influence
						SSC-A09	2, 4	0·2, 0·4	15 ± 10	0·01		studies
Niu *et al.*[19]	MUSCL + limiter	RK $O(\Delta t^2)$	249 × 64			NACA 0012	4	0·3	15 ± 10	0·15	($c/4$)	Also $k = 1{\cdot}5$

eddy viscosity without resorting to empirical length scale specifications. The so-called k–ε model is the most often used, sometimes in conjunction with wall functions.[18] The wall function approach allows significant savings in grid points (since the first grid points lie at about $y^+ = 50$–200 instead of $y^+ \approx 1$) but is clearly inadequate when flow separation is present. It is also remarkable that the results show considerable differences depending on the type of second turbulence equation used (e.g. ε- or ω-equation[15,17]).

Among the considered test cases, the well-known NACA 0012 aerofoil is the most often studied, one of the historical reasons being that a conformal grid can be specified for it analytically and another reason being that detailed dynamic stall experiments[24–27] have often been conducted on this case. Of course, other aerofoils can be treated as well with the development of numerically generated boundary-fitted grids. The design of the grid surrounding the aerofoil is performed in general using elliptic grid generation techniques, although conformal mapping techniques allow an elegant way of providing an adequate orthogonal (and particularly smooth) grid,[11,12,14] a hyperbolic grid generation technique being used in Reference 13. Most topologies are of the O- or C-type, while the number of grid points shows a marked tendency to increase with the available computer resources. The flow domain and the grid resolution depend on the Reynolds and Mach numbers of the considered test cases and best results are associated with a boundary layer grid resolution placing the first points away from the wall at a distance of the order of some integer value of $10^{-5}c$.

The paper is organized as follows. The flow equations and numerical aspects are presented in Sections 2 and 3 respectively together with the turbulence models used. Some examples of calculations of the turbulent flow past an aerofoil oscillating sinusoidally in pitch are presented in Section 4.

2. GOVERNING EQUATIONS

The unsteady incompressible Reynolds-averaged Navier–Stokes equations can be written as

$$\nabla\cdot\mathbf{U} = 0, \tag{1}$$

$$\frac{\partial\mathbf{U}}{\partial t} + \nabla\cdot\mathbf{F} = \sigma, \tag{2}$$

with the Cartesian components

$$\bar{F}_{kj} = \bar{U}_k\bar{U}_j + P\delta_{kj} - \frac{1}{R_{\mathrm{eff}}}\frac{\partial\bar{U}_k}{\partial x_j} - \nu_{\mathrm{T}}\frac{\partial\bar{U}_j}{\partial x_k} - \delta_{jk}\frac{\Omega^2 r^2}{2} - \varepsilon_{kij}\frac{r^2}{2}\frac{\mathrm{d}\Omega_i}{\mathrm{d}t}, \tag{3a}$$

where

$$\frac{1}{R_{\mathrm{eff}}} = \frac{1}{Re} + \nu_{\mathrm{T}}, \qquad P = \rho^{-1}p + \tfrac{2}{3}K, \qquad \sigma_1 = 2\Omega\bar{U}_2, \qquad \sigma_2 = -2\Omega\bar{U}_1. \tag{3b}$$

They involve the mean Cartesian velocity components $\{\bar{U}_k\}$ relative to orthonormal axes moving with the aerofoil, the mean pressure p, the Reynolds number $Re = U_\infty c/\nu$ (where U_∞ is the freestream velocity, c is the aerofoil chord and ν is the kinematic viscosity of the fluid) and the Kronecker symbol δ_{kj}. The two last terms (3a) involving the angular velocity ω of the aerofoil are the Euler acceleration and the centripetal acceleration. From now on, summation over repeated indices is assumed unless specified otherwise. R_{eff} is the so-called effective Reynolds number. The source term σ is due to the Coriolis force $2\mathbf{\Omega} \times \mathbf{U}$, but we have made the additional assumption that the flow is two-dimensional in the plane $\{x_1, x_2\}$, while Ω is along x_3. Equation (3) has been obtained assuming a linear eddy viscosity hypothesis for the turbulent Reynolds stresses:

$$-\overline{\mathbf{u}'\mathbf{u}'} = -\tfrac{2}{3}K\mathbf{I} + \nu_{\mathrm{T}}(\nabla\mathbf{U} + \nabla^{\mathrm{T}}\mathbf{U}), \tag{4}$$

where $K = \overline{u'^2}/2$ is the so-called turbulent kinetic energy and ν_{T} is the turbulent eddy viscosity which defines the eddy viscosity model to be used. In this work, two models have been tested: the Baldwin–Barth model[23] in which an additional equation is written for the turbulent Reynolds number defined from ν_{T}, and the so-called K–ω SST model[28] which solves two transport equations, one for the turbulent kinetic energy K and the other for ω which has the dimensions of frequency.

For the applications to be considered, the complexity of the geometry prevents the use of Cartesian co-ordinates. Numerical co-ordinate transformations are required in order to facilitate the application of boundary conditions and transform the physical domain in which the flow is studied into a rectangular domain $\{\xi^1, \xi^2\}$. This computational domain consists of a set of unique squares of sides $\Delta\xi^i = 1$, $i = 1, 2$. Each unit square in the computational domain is a curvilinear quadrilateral in the physical plane, the sides of which are measured by the moduli of the covariant vectors $\mathbf{a}_i = \partial\mathbf{R}/\partial\xi^i$. The transformation involves by-products from the covariant basis. Of particular interest are the following: (i) the area vectors $\mathbf{b}_i = \mathbf{a}_j \times \mathbf{a}_k$ (i, j, k in cyclic order) which measure the oriented area (per unit span) of a small surface of unit sides along ξ^i and ξ^k on a $\xi^i = \text{const.}$ surface in the computational space, where $\mathbf{b}_i = J^{-1}\,\mathbf{grad}\xi^i$ is constructed from two small triangle-like surfaces in the physical space; (ii) the Jacobian J of the transformation from the computational space of the co-ordinates $\{\xi^i\}$ to the physical space of the Cartesian co-ordinates $\{x_i\}$, which measures the 'physical' volume of a unit cube in the computational space and is evaluated in such a way that $\mathbf{a}_i\cdot\mathbf{b}^j = J\delta_i^j$; (iii) the covariant and contravariant metric tensors $g_{ij} = \mathbf{a}_j\cdot\mathbf{a}_k$ and $g^{ij} = g^{-1}\mathbf{b}^i\cdot\mathbf{b}^j$, where g, the determinant of g_{ij}, is the square, J^2, of the previously defined Jacobian.

Using the chain rule derivative formula $\partial\xi^k/\partial x_i = J^{-1}b_i^k$, we obtain

$$\nabla\cdot\mathbf{U} = J^{-1}\frac{\partial(JU^i)}{\partial\xi^i} = J^{-1}\frac{\partial(b_k^i\bar{U}_k)}{\partial\xi^i}, \tag{5}$$

where U^i is the contravariant velocity component $\mathbf{U}\cdot\mathbf{b}^i/J$ (equivalently the mass flux is JU^i). If $\bar{U}_i = \delta_k^i$, with $k = 1, 2$, equation (4) yields the so-called first geometric conservation law which can be expressed as follows: when properly discretized, areas of a discrete cell will sum to the total volume. The momentum equation (2) is written in the strong conservation form

$$\frac{\partial\bar{U}_k}{\partial t} + \frac{1}{J}\frac{\partial(b_j^i\bar{F}_{kj})}{\partial\xi^i} = \sigma_k, \tag{6}$$

with

$$\bar{F}_{kj} = \bar{U}_k\bar{U}_j + P\delta_{kj} - \frac{b_j^m}{JR_{\mathrm{eff}}}\frac{\partial\bar{U}_k}{\partial\xi^m} - \frac{\nu_{\mathrm{T}}}{J}b_k^m\frac{\partial\bar{U}_j}{\partial\xi^m} - \delta_{jk}\frac{\Omega^2r^2}{2} - \varepsilon_{kij}\frac{r^2}{2}\frac{\mathrm{d}\Omega_i}{\mathrm{d}t}. \tag{7}$$

The convective form

$$\begin{aligned}
&\frac{\partial\bar{U}_k}{\partial t} + \left(U^i - \frac{f^i}{R_{\mathrm{eff}}} - g^{in}\frac{\partial\nu_{\mathrm{T}}}{\partial\xi^n}\right)\frac{\partial\bar{U}_k}{\partial\xi^n} + J^{-1}b_m^i\frac{\partial P}{\partial\xi^m}\\
&\quad = \frac{g^{ij}}{R_{\mathrm{eff}}}\frac{\partial^2\bar{U}_k}{\partial\xi^i\partial\xi^j} + J^{-2}b_j^nb_k^m\frac{\partial\nu_{\mathrm{T}}}{\partial\xi^n}\frac{\partial\bar{U}_j}{\partial\xi^m} + J^{-1}\frac{\partial}{\partial\xi^i}b_k^i\frac{\Omega^2r^2}{2} - \varepsilon_{kjp}J^{-1}\frac{\mathrm{d}\Omega_p}{\mathrm{d}t}\frac{\partial}{\partial\xi^i}\left(\frac{r^2}{2}b_j^i\right) + \sigma k
\end{aligned} \tag{8}$$

will also prove necessary in what follows, where

$$f^i = \frac{1}{J}\frac{\partial}{\partial\xi^m}\left(\frac{\mathbf{b}^i\cdot\mathbf{b}^m}{J}\right) \tag{9}$$

specifies the so-called stretching functions.

3. NUMERICAL METHOD

3.1. Grid lay-out and discrete equations

The so-called collocated cell-centred grid lay-out is used: the Cartesian velocity components and the pressure share the same location at the centre of the control volume D (Figure 1). Owing to its non-standard character, it is useful to make notation conventions implicit. Neighbours of the point NN at the centre of the control volume are identified by two uppercase letters: the first is relative to the direction ξ^1, the second to the direction ξ^2 such that the body wall is given by $\xi^2=0$. Points are identified with the letters M (minus one), P (plus one) and N (null). The fluxes JU^i are located on the faces of the control volume (identified by a lowercase letter) in the direction of the normal to the face. Grid points are located at the centres of the control volume D. In the following, $\bar{U}_k$(NN) will be the unknown kth Cartesian velocity component at point NN. The flux at cell interface pN is identified as (JU^i)(pN). Although non-standard, the present notation allows a straightforward coding of the method, particularly in the three-dimensional case.

The discrete divergence of the flux ϕ over the control volume D is simply

$$(\Delta_i\Phi^i)(\mathrm{NN}) = \Phi^1(\mathrm{pN}) - \Phi^1(\mathrm{mN}) + \Phi^2(\mathrm{Np}) - \Phi^2(\mathrm{Nm}), \tag{10}$$

so that the discrete continuity equation results from $\phi = J\mathbf{U}$.

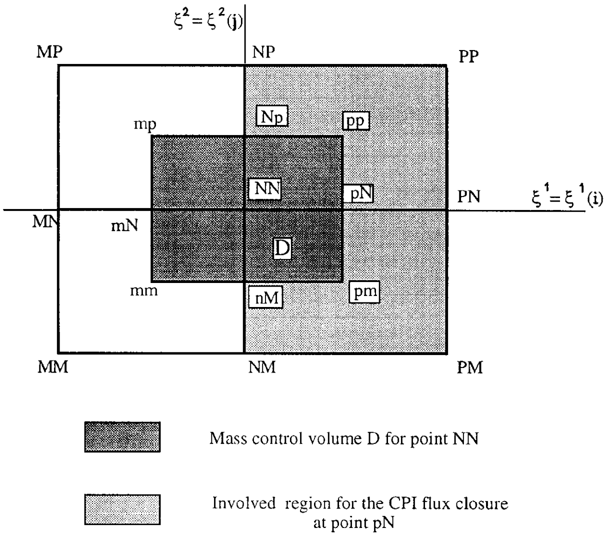

Figure 1. Schematic sketch of presently used notation and influence stencil of point NN for CPI method

The time derivative is discretized using a second-order-accurate backward Euler method involving the time levels $t^0 = t - \delta t$ and $t^{00} = t - 2\delta t$ besides the actuual time level t. We then have

$$\begin{aligned} &\frac{\partial\phi}{\partial t} \approx e_1\Phi + e_0\Phi^0 + e_{00}\Phi^{00}, \\ &e_1 = \frac{3}{2\Delta t}, \qquad e_0 = -\frac{2}{\Delta t}, \qquad e_{00} = \frac{1}{2\Delta t}, \\ &\Phi \approx \phi(t), \qquad \Phi^0 = \phi(t^0), \qquad \Phi^{00} \approx \phi(t^{00}). \end{aligned} \tag{11}$$

Using (10) and (11) yields the motion equations

$$\frac{1}{J(\mathrm{NN})}\Delta_i(b^i_j\bar{U}_j)(\mathrm{NN}) = 0, \tag{12}$$

$$e_1\bar{U}_k(\mathrm{NN}) + e_0\bar{U}^0_k(\mathrm{NN}) + e_{00}\bar{U}^{00}_k(\mathrm{NN}) + \frac{1}{J(\mathrm{NN})}\Delta_i(b^i_j\bar{F}_{kj})(\mathrm{NN}) = \sigma_k(\mathrm{NN}) \tag{13}$$

In the discrete divergence at point NN in (13) the linearized momentum flux $\mathbf{b}^i\cdot\bar{\mathbf{F}}_k$ is defined at interfaces pN, mN, Np and Nm as indicated in (10). For instance,

$$\mathbf{b}^i\cdot\bar{\mathbf{F}}_k(\mathrm{pN}) = \left[(\mathbf{b}^i\cdot\mathbf{U}^*)\bar{U}_k + Pb^i_k - \frac{\mathbf{b}^i\cdot\mathbf{b}^m}{R_{\mathrm{eff}}J}\frac{\partial\bar{U}_k}{\partial\xi^m} - \frac{\nu_{\mathrm{T}}}{J}b^i_j b^m_k\frac{\partial\bar{U}_j}{\partial\xi^m} - b^i_k\frac{\Omega^2 r^2}{2} - \frac{r^2}{2}\left(\mathbf{b}^i\times\frac{\mathrm{d}\Omega}{\mathrm{d}t}\right)_k\right](\mathrm{pN}), \tag{14}$$

where $\mathbf{U}^*$ is a prediction of the velocity field at the actual time. An iterative procedure is thus required at time t in order to update $\mathbf{U}^*$, starting with $\mathbf{U}^* = \mathbf{U}_0$. The approximation of (14) and of similar fluxes at mN, nP and Nm is carried out so that the resulting discrete momentum equations are centred. For instance, with $i = 1$,

$$\begin{aligned} \mathbf{b}^1\cdot\bar{\mathbf{F}}_k(\mathrm{pN}) \approx\; & c_1(\mathrm{pN})\bar{U}_k(\mathrm{pN}) + \tfrac{1}{2}b^1_k(\mathrm{pN})[P(\mathrm{PN}) + P(\mathrm{NN})] - d_{11}(\mathrm{pN})[\bar{U}_k(\mathrm{pN}) - \bar{U}_k(\mathrm{NN})] \\ & - \tfrac{1}{4}d_{11}(\mathrm{pN})[\bar{U}_k(\mathrm{PP}) + \bar{U}_k(\mathrm{NP}) - \bar{U}_k(\mathrm{PM}) - \bar{U}_k(\mathrm{NM})] \\ & + \beta^{11}_{1k}[\bar{U}_1(\mathrm{pN}) - \bar{U}_1(\mathrm{NN})] + \beta^{11}_{2k}[\bar{U}_2(\mathrm{pN}) - \bar{U}_2(\mathrm{NN})] \\ & + \beta^{12}_{1k}[\bar{U}_1(\mathrm{PP}) + \bar{U}_1(\mathrm{NP}) - \bar{U}_1(\mathrm{PM}) - \bar{U}_1(\mathrm{NM})] \\ & + \beta^{12}_{2k}[\bar{U}_2(\mathrm{PP}) + \bar{U}_2(\mathrm{NP}) - \bar{U}_2(\mathrm{PM}) - \bar{U}_2(\mathrm{NM})] \\ & - \left[b^1_k\frac{\Omega^2 r^2}{2} - \frac{r^2}{2}\left(\mathbf{b}^1\times\frac{\mathrm{d}\Omega}{\mathrm{d}t}\right)_k\right](\mathrm{pN}), \end{aligned} \tag{15}$$

where $c_i = \mathbf{b}^i\cdot\mathbf{U}^*$, $d_{im} = \mathbf{b}^i\cdot\mathbf{b}^m/R_{\mathrm{eff}}J$ and $\beta^{im}_{jk} = J^{-1}\nu_{\mathrm{T}}b^i_j b^m_k$ are evaluated at pN for $i = 1, 2$. Similar expressions are obtained at other face points mN, Np and Nm.

3.2. Reconstruction problem and its formal solution

It appears that besides unknown nodal values of the Cartesian velocity components, expressions such as (15) involve the values $\bar{U}_k(\mathrm{pN})$ which are also unknown, but at points which are not nodal points. This introduces the so-called reconstruction problem: fluxes such as $\bar{U}_k(\mathrm{pN})$ which are not defined at nodal points must be expressed in terms of nodal unknowns. The interpolation procedure which solves the reconstruction problem must avoid spurious pressure modes which may exist when collocated grids are used. One of the most efficient ways to overcome this difficulty is to use a physical interpolation approach in which a velocity integration points value such as $\bar{U}_k(\mathrm{pN})$ is expressed not only in terms of values of $\bar{U}_k$ at the neighbouring nodes of pN, the set of which (Figure 1) is denoted $NB(\text{pN}) = \{\text{NN, PN, PM, PP, NP, NM}\}$ (the reason for this choice of neighbouring nodes will be justified later), but also in terms of values of other velocity components and pressure at NB(pN). The most classical approach in this respect is the Rhie and Chow interpolation.[29] Its drawbacks, as well as those of another interpolation practice due to Schneider and Raw,[30] have been analysed in References 31 and 32, where the so-called consistent physical interpolation (CPI) method is proposed. The application of the CPI method to unsteady laminar flows has been further developed in Reference 33 for aerofoil problems.

3.3. *CPI method*

The CPI method determines $\bar{U}_k(\text{pN})$ from the solution of the convective form of the momentum equations at point pN. This interpolation involves the set of neighbours NB(pN) of influencing nodes (Figure 1). The result can be written at pN as the following explicit expression in $\bar{U}_k(\text{pN})$,

$$(e_1 + D_{\text{pN}})\bar{U}_k(\text{pN}) = \sum_{NB(\text{pN})} C^U_{NB(\text{pN})}\bar{U}_k[NB(\text{pN})] + \sum_{NB(\text{pN})} C^{Pk}_{NB(\text{pN})}P[NB(\text{pN})] + S_k(\text{pN}), \tag{16}$$

and in a similar way at mN, Np and Nm. For the other interfaces of the control volume D the sets of active neighbours are

$$\begin{aligned} NB(\text{mN}) &= \{\text{MN, NN, MP, NP, MM, MN}\},\\ NB(\text{Np}) &= \{\text{NN, NP, NM, PM, PN, PP}\},\\ NB(\text{Nm}) &= \{\text{NN, PN, MN, PM, NM, MM}\}. \end{aligned}$$

The influence coefficients satisfy the consistency conditions

$$\sum_{NB(\text{pN})} C^U_{NB(\text{pN})} = D_{\text{pN}}, \qquad \sum_{NB(\text{pN})} C^{Pk}_{NB(\text{pN})} = 0, \quad k = 1, 2. \tag{17a,b}$$

The former relation (17a) indicates that $\bar{U}_k(\text{pN})$ involves a weighted interpolation of $\bar{U}_k$ at neighbouring nodal values denoted NB(pN). The latter relation (17b) corresponds to the fact that the summation over pressure values is of the gradient type. It can be shown that the CPI yields second-order accuracy on a uniform Cartesian grid,[32] with an adequate upwinding effect for both velocities and pressure.[31] We shall require the generalized form

$$(e_1 + D_f)\bar{U}_k(f) = \sum_{NB(f)} C^U_{NB(f)}\bar{U}_k[NB(f)] + \sum_{NB(f)} C^{Pk}_{NB(f)}P[NB(f)] + S_k(f), \quad f = \text{pN, mN, Np, Nm}, \tag{16$'$}$$

in what follows. Equation (16′) can be viewed as a definition of the so-called pseudovelocity

$$\hat{U}_k(f) = \frac{1}{e + 1 + D_f}\{C^U_{NB(f)}\bar{U}_k[NB(f)] + S_k(F)\} \tag{18a}$$

such that

$$\bar{U}_k(f) = \hat{U}_k(f) + \frac{1}{e_1 + D_f}\left(\sum_{NB(f)} C^{Pk}_{NB(f)}P[NB(f)]\right). \tag{18b}$$

We still have to demonstrate how the expression of the influence coefficients C^U and C^{Pk} and of the source term S_k in (18) can be obtained from a discrete scheme for the momentum equation written at $f = $ pN, mN, Np, Nm. This will now be explained for the fluxes at point pN using the momentum equation written at pN. The retained discrete scheme is the so-called multiexponential scheme, which consists of using an exponential scheme[32] in both directions. The scheme is applied to the convective form of the momentum equation (8) and the result written at pN is a slight extension of what was already obtained in Reference 33, namely

$$\begin{aligned}(e_1 + C_{\mathrm{N1}} + C_{\mathrm{N2}})\bar{U}_k(\mathrm{pN}) + C_{\mathrm{P1}}\bar{U}_k(\mathrm{PN}) + C_{\mathrm{M1}}\bar{U}_k(\mathrm{NN}) + \tfrac{1}{2}C_{\mathrm{P2}}[\bar{U}_k(\mathrm{NP}) + \bar{U}_k(\mathrm{PP})] + \tfrac{1}{2}C_{\mathrm{M2}}[\bar{U}_k(\mathrm{NM})\\ + \bar{U}_k(\mathrm{PM})]\\ = \left(\frac{g^{ij}}{R_{\mathrm{eff}}}\frac{\partial^2\bar{U}_k}{\partial\xi^i\partial\xi^j}\bigg|_{i\neq m} + J^{-2}b_j^n b_k^m\frac{\partial\nu_{\mathrm{T}}}{\partial\xi^n}\frac{\partial\bar{U}_j}{\partial\xi^m} - J^{-1}b_m^i\frac{\partial P}{\partial\xi^m}\right)(\mathrm{pN})\\ - \left[b_k^1\frac{\Omega^2 r^2}{2} - \frac{r^2}{2}\left(\mathbf{b}^1\times\frac{\mathrm{d}\Omega}{\mathrm{d}t}\right)_k\right](\mathrm{pN}) - e_0\bar{U}_k^0(\mathrm{pN}) - e_{00}\bar{U}_k^{00}(\mathrm{pN}),\end{aligned} \tag{19}$$

where the influence coefficients are

$$C_{\mathrm{P}i} = \frac{K_i}{\exp(\gamma_i) - 1}, \qquad C_{\mathrm{M}i} = \frac{K_i\exp(\gamma_i)}{\exp(\gamma_i) - 1}, \qquad C_{\mathrm{N}i} + C_{\mathrm{M}i} + C_{\mathrm{P}i} = 0, \quad i = 1, 2,$$

which involve the convective coefficients K_i, the previously defined diffusion coefficients d_{ij} at pN along the direction i and the mesh Peclet numbers γ_i:

$$K_i = \left(U^i - \frac{f^i}{R_{\mathrm{eff}}} - g^{in}\frac{\partial\nu_{\mathrm{T}}}{\partial\xi^n}\right)(\mathrm{pN}), \qquad \gamma_i = \frac{K_i h_i}{d_{ii}}.$$

(Notice that on curvilinear grids the grid spacings h_i along ξ^i can be taken equal to 1, except close to the boundaries where they may take the value $\frac{1}{2}$). The second-order cross-derivative terms in (19) are treated using a centred scheme

$$\left(d_{ij}\frac{\partial^2\bar{U}_k}{\partial\xi^i\partial\xi^j}\bigg|_{i\neq m}\right)(\mathrm{pN}) \approx \frac{1}{4h_1h_2}d_{12}(\mathrm{pN})[\bar{U}_k(\mathrm{PP}) + \bar{U}_k(\mathrm{NP}) - \bar{U}_k(\mathrm{PM}) + \bar{U}_k(\mathrm{NM})], \tag{20}$$

as are other first-derivative velocity terms. Finally, the pressure gradient at pN in (19) is centred at pN:

$$J^{-1}b_m^1\frac{\partial P}{\partial\xi^1} \approx \frac{1}{2h_1}(J^{-1}b_m^1)(\mathrm{pN})[P(\mathrm{PN}) - P(\mathrm{NN})], \tag{21a}$$

$$J^{-1}b_m^2\frac{\partial P}{\partial\xi^2} \approx \frac{1}{4h_2}(J^{-1}b_m^2)(\mathrm{pN})[P(\mathrm{PP}) + P(\mathrm{NP}) - P(\mathrm{PM}) - P(\mathrm{NM})]. \tag{21b}$$

The resulting influence coefficients in (17) are obtained by substitution of (20) and (21) into (19).

3.4. *Equations for nodal unknowns*

Upon substitution of closures (16′) written at pN, mN, nP and nM into the discrete momentum equation (13), where relations such as (14) and (15) have been accounted for, we obtain the following discrete scheme for the momentum equations corresponding to $k = 1$, 2:

$$[e_1 + D^U(\mathrm{NN})]\bar{U}_k(\mathrm{NN}) = \sum_{NB(\mathrm{NN})} K^U_{NB(\mathrm{NN})}\bar{U}_k[NB(\mathrm{NN})] + \sum_{NB(\mathrm{NN})} K^{kP}_{NB(\mathrm{NN})}P[NB(\mathrm{NN})] + \Sigma_k(\mathrm{NN}), \tag{22}$$

where the velocity and pressure unknowns are located only at NN and at the eight nodal neighbours of the set $NB(\mathrm{NN}) = \{\mathrm{MM, MN, MP, NM, NP, PM, PN, PP}\}$; the summations are over the eight corresponding contributions. The influence coefficients $K^{kP}_{NB(\mathrm{NN})}$ involved in the summation for the pressure terms result from the identity

$$\sum_{NB(\mathrm{NN})} K^{kP}_{NB(\mathrm{NN})} P[NB(\mathrm{NN})] = \frac{1}{J(\mathrm{NN})}\Delta_f\left(b^f_k + \frac{K_f}{e_1+D_f}\sum_{NB(f)} C^{Pk}_{NB(\mathrm{NN})}P[NB(f)]\right). \tag{23}$$

The substitution of closures like (16′) into the continuity equation (12) yield similarly, from a pressure equation of the form

$$\frac{1}{J(\mathrm{NN})}\Delta_f\left[\frac{b^f_k}{e_1+D_f}\left(\sum_{NB(\mathrm{NN})} C^{U}_{NB(f)}\bar{U}_k[\mathrm{NB}(f)] + \sum_{NB(f)} C^{Pk}_{NB(f)}P[NB(f)] + S_k(f)\right)\right] = 0, \tag{24a}$$

the discrete pressure equation

$$\sum_{NB(\mathrm{NN})} K^{Pk}_{NB(f)}\bar{U}_k[NB(\mathrm{NN})] + \sum_{NB(\mathrm{NN})} K^{PP}_{NB(\mathrm{NN})}P[NB(\mathrm{NN})] + \Sigma_P(\mathrm{NN}). \tag{24b}$$

Equation (24a) can be viewed as a pressure equation if the substituted closure takes the form of (18b) instead of (16′):

$$\mathrm{div}(\nabla P) \equiv \frac{1}{J(\mathrm{NN})}\Delta_f\left[\frac{b^f_k}{e_1+D_f}\left(\sum_{NB(f)} C^{Pk}_{NB(f)}P[NB(f)]\right)\right] = -\mathrm{div}\hat{\mathbf{U}} \equiv -\frac{1}{J(\mathrm{NN})}\Delta_f[b^f_k\hat{U}_k(f)]. \tag{25}$$

The two momentum equations (22) ($k=1$, 2) and equation (24b) written at each inner point NN(i, j) in the computational space generate the system of unknowns. We group the three unknowns $\bar{U}_1$, $\bar{U}_2$ and P at each grid point (i, j) to define a vector

$$\mathbf{X}(i,j) \equiv \|\bar{U}_1(i,j),\quad \bar{U}_2(i,j),\quad P(i,j)\|^{\mathrm{T}}$$

with three components and we order the unknowns from values $i=1$ to $i_{\max}$ and, for any given value of i, from $j=1$ to $j_{\max}$. When the $i(j-1)$th, ijth and $i(j+1)$th rows of the matrix **A** corresponding to (22) ($k=1$), (22) ($k=2$) and (24b) are also grouped in this order, the matrix **A** appears as a block 3 × 3 nine-diagonal matrix whose non-vanishing elements in the ijth block 3 × 3 row are located on the $(i-1)(j-1)$th, $(i-1)j$th, $(i-1)(j+1)$th columns (influence coefficients of points MM(i, j), MN(i, j), MP(i, j) respectively), on the $i(j-1)$th, ijth, $i(j+1)$th columns (influence coefficients of points NM(i, j), NN(i, j), NP(i, j) respectively) and on the $(i+1)(j-1)$th, $(i+1)j$th, $(i+1)(j+1)$th columns (influence coefficients of points PM(i, j), PN(i, j), PP(i, j) respectively). This demonstrates the optimal compactness of the CPI method which essentially results from the retained sets of flux point neighbours like *NB*(pN).

3.5. *Pressure–velocity coupling algorithm*

The algorithm which yields a coupled solution of the system (22), (25) is directly inspired by the PISO algorithm[34] and consists of the following steps.

1. Initiate the velocity field and the pressure field at time t^0.
2. New time step $t=t+\Delta t$.
3. Start iterative procedure with $\bar{U}_k=\bar{U}^0_k$, $P=P^0$, $\bar{U}_k(f)=\bar{U}^0_k(f)$.
4. Compute the reconstruction coefficients from the field of step 3.
5. Solve the momentum equations to obtain a new prediction for $\bar{U}_k$.
6. Solve the continuity equation to obtain pressure P with coefficients obtained from step 4 and $\bar{U}_k$ from step 5.

7. Correct the velocity field with coefficients from step 4, $\bar{U}_k$ from step 3 and P from step 6.
8. Reconstruction at interfaces to get $\bar{U}_k(f)$ with coefficients from step 4, P from step 6 and $\bar{U}_k$ from step 7.
9. If non-linear residuals are low enough, go to step 1 and update t; otherwise, go to step 3 and update the iteration count within time step t.

4. RESULTS

Before presenting results, some numerical parameters need to be specified. For each time step a reduction by one order of magnitude of non-linear residuals of discrete momentum equations is required. Also, the divergence of the velocity field is decreased to between 10^{-6} and 10^{-10} with the BB model and to between 10^{-7} and 10^{-9} with the K–ω model. Turbulence equations see their non-linear residuals lowered by at least two orders of magnitude for the turbulent Reynolds number equation of the BB model and for the two equations in the K–ω model, except for the K-equation at the beginning of the upstroke: non-linear residuals are then decreased by only one order of magnitude at each time step. A general trend is that the CPU cost per time step increases with decreasing reduced frequency for a fixed value of Δt^*. The CPU cost per time step also increases with increasing $\Delta\alpha$. Some results concerning the influence of the grid size and of the time step are given in Figure 9 of the Appendix. The presented results focus on the second period of oscillations: extensive tests have shown that, in contrast with the findings of Raffel *et al.*,[35] the repeatability of calculations is good between the second cycle and the following ones (see Figure 10 of Appendix).

We consider the flow past aerofoils oscillating in pitch with the incidence law

$$\alpha = \alpha_0 + \Delta\alpha \cos(2\pi f t) = \alpha_0 + \Delta\alpha \cos(2kt^*),$$

where k is the reduced frequency and $t^* = tU_\infty/c$ is the non-dimensional time defined from the chord c of the aerofoil. The reduced frequency is the most influential parameter of dynamic stall: it represents the ratio of two time scales, one imposed by the pitching motion, $(2\pi f)^{-1}$, and the other by the freestream velocity and the half-chord, $c/2U_\infty$.

Case 1

The first case considered is that of an NACA 0012 aerofoil with $\alpha_0 = 15°$, $\Delta\alpha = 10°$, $k = 0{\cdot}15$ and $Re = 10^6$, for which experimental data[27] corresponding to the 'deep stall' case of McAlister *et al.* are available. Because of the particularly high values of α_0 and $\Delta\alpha$, this case has so far been considered only in References 11, 12 and 18. The non-dimensional period of motion is $T^* = 20{\cdot}94$, with 4190 time steps per cycle for $\Delta t^* = 0{\cdot}005$. Two models have been tested, the so-called BB model and the K–ω SST model.

We consider the sequence of events starting from the incidence 0° (Figures 2(a)–2(u)). In agreement with the experimental data,[35] the flow remains attached up to an incidence of about 18°. The instantaneous streamlines at 15° (Figure 2(c)) are still indicative of fully attached flow, in good agreement with the data[35] at 17°, for $Re = 3{\cdot}73 \times 10^5$. Thus there is a significant delay of stall to higher incidences with respect to that ($\alpha_s \approx 16°$) found at fixed incidence. Separation occurs around 20° (Figure 2(d)), while experiments[36] which involve the same motion but $Re = 2{\cdot}5 \times 10^6$ find it at $\alpha = 19°$–$20°$. As the aerofoil leading edge moves upwards, the boundary layer between stagnation and separation experiences a moving wall jet effect. The boundary layer has a fuller velocity profile as compared with the steady case and is therefore more resistant to separation (on the downstroke the effect will be the opposite, promoting separation). As the incidence increases (Figures 2(e)–2(i)), a dynamic stall vortex (DSV) develops in both cases near the leading edge, although later with the K–ω

2 a) α=5.0 deg up

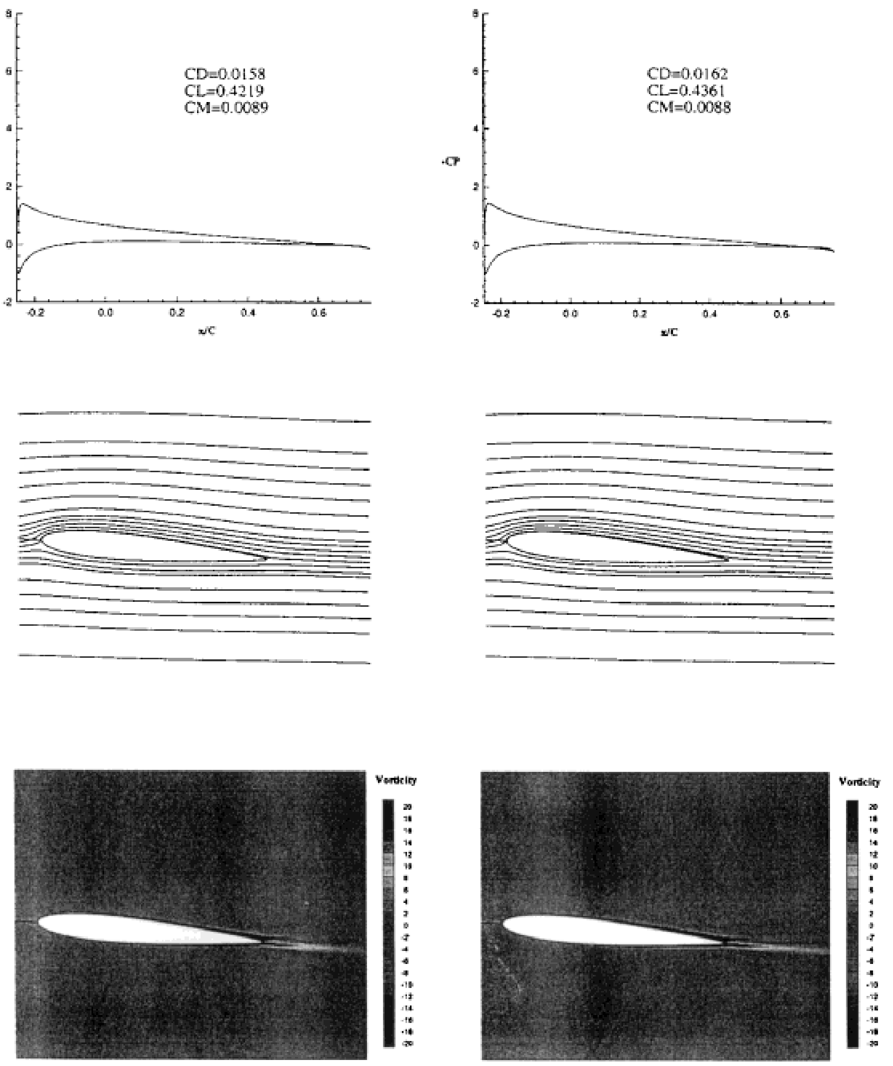

Figure 2(a)–2(u). Flow past NACA 0012. $Re = 10^6$, $k = 0{\cdot}15$. Comparison between calculations performed with BB model and K–ω SST model. 200 × 90 O-type conformal grid. $\delta t^* = 0{\cdot}005$. Incidences are indicated. Upper part, wall pressure coefficient; middle part, relative streamlines; lower part, instantaneous mean vorticity field. Instantaneous force coefficients are also indicated. Left, BB model; right, K–ω model. Time instants at which the flow is plotted in Figure 4 are specified by a letter

2 b) α=10.0 deg up

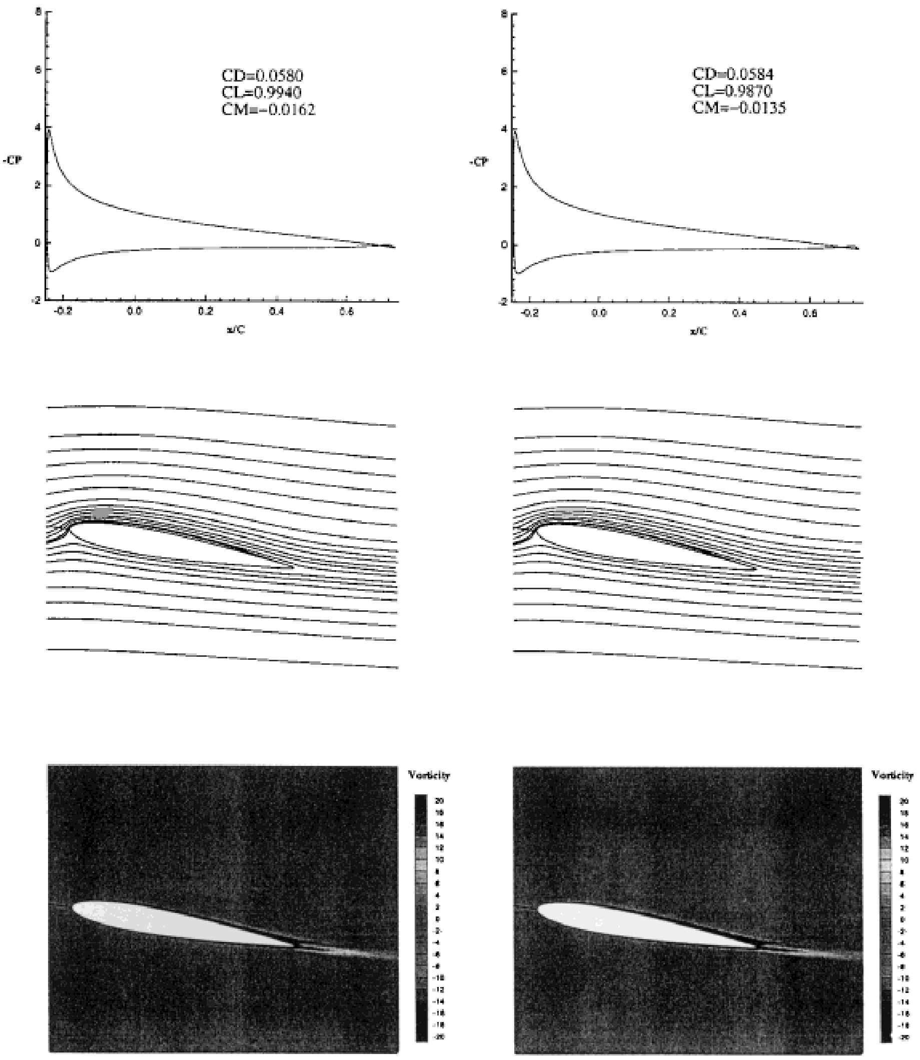

Figure 2 (*continued*)

2 c) α=15.0 deg up

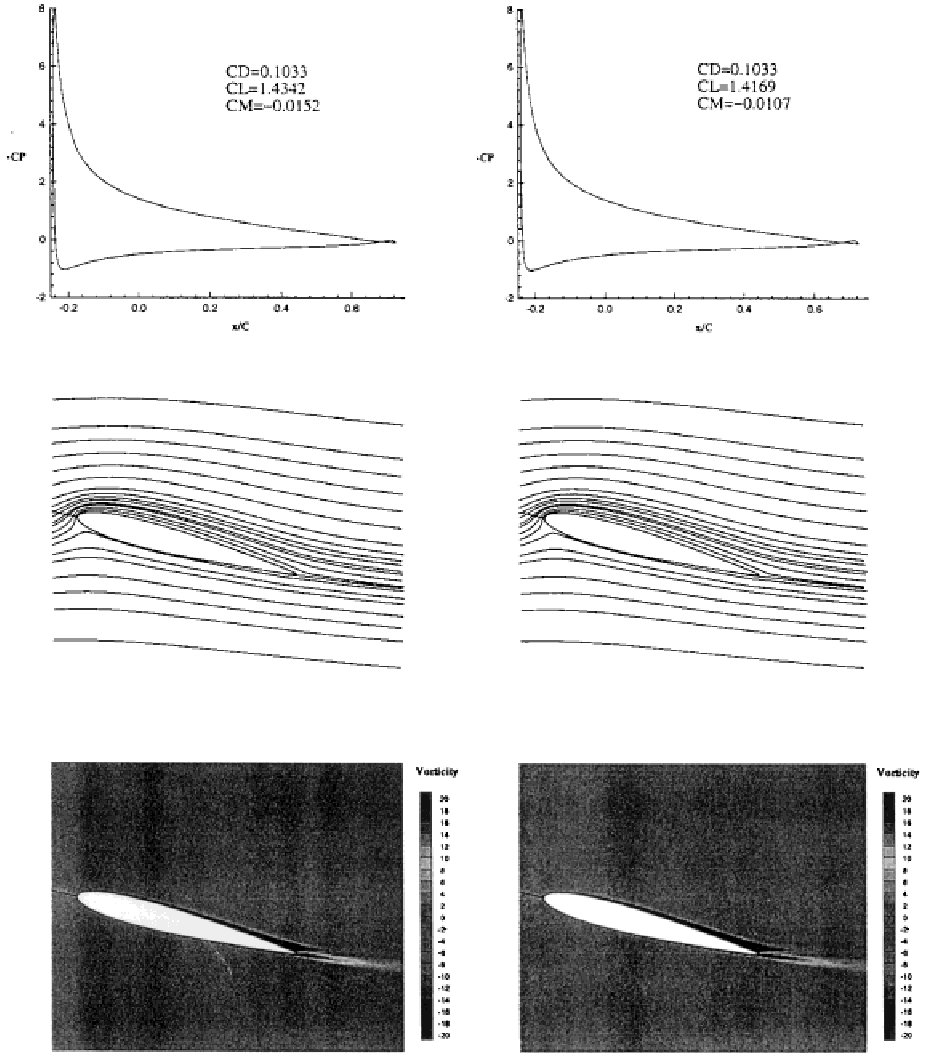

Figure 2 (*continued*)

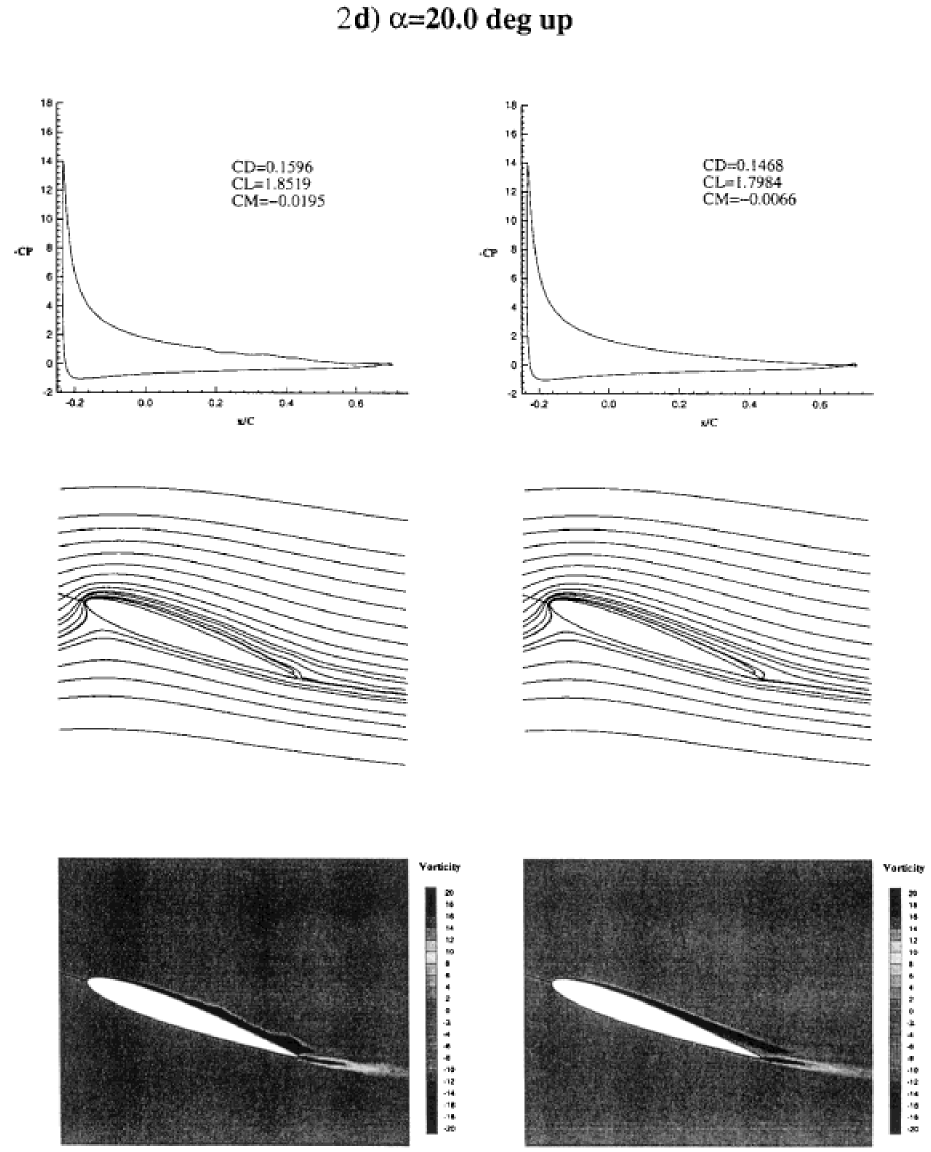

Figure 2 (*continued*)

2e) α=22.5 deg up

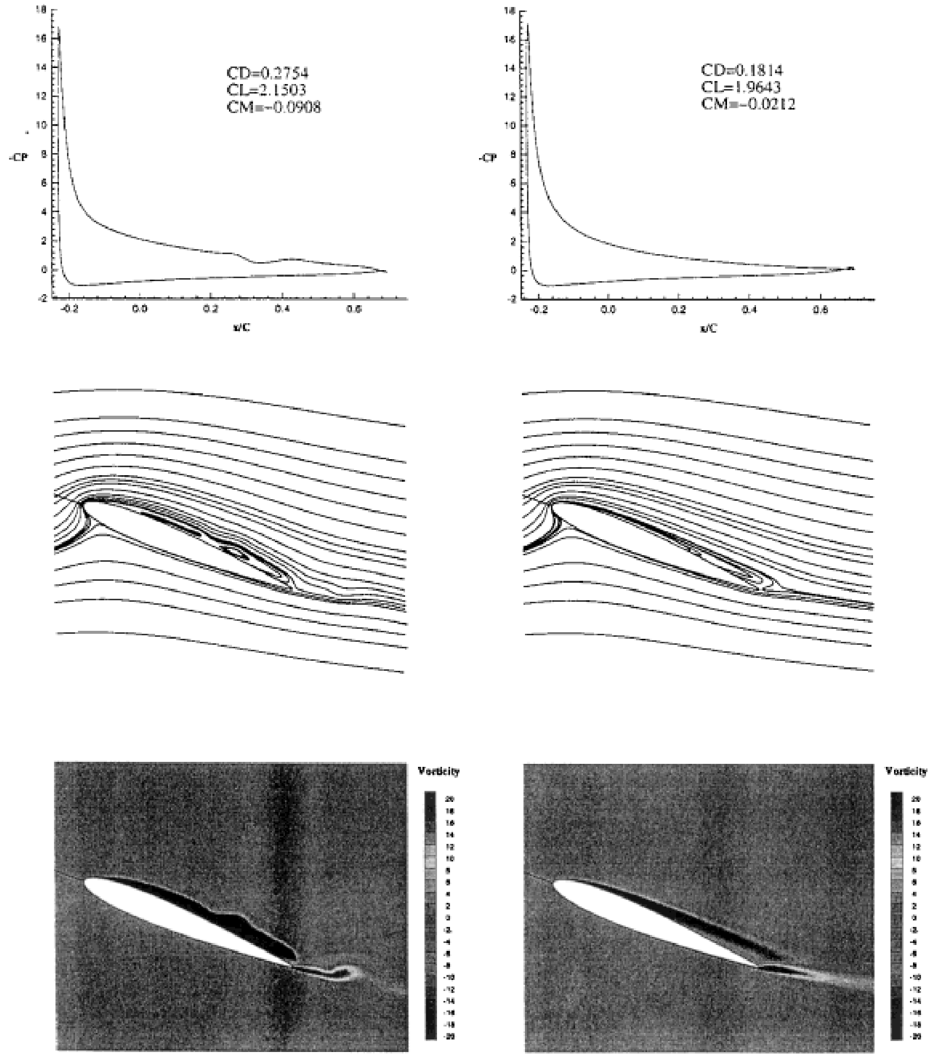

Figure 2 (*continued*)

2f) α=23.6 deg up

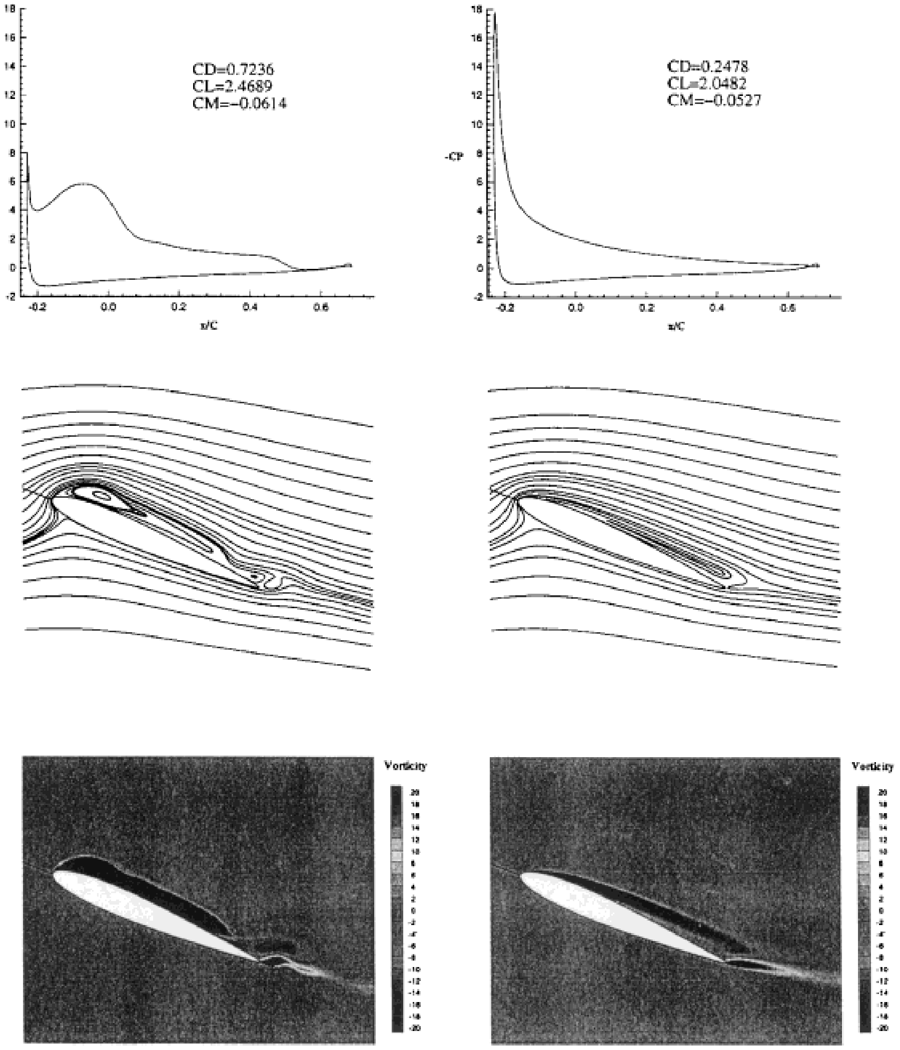

Figure 2 (*continued*)

2g) α=24.2 deg up

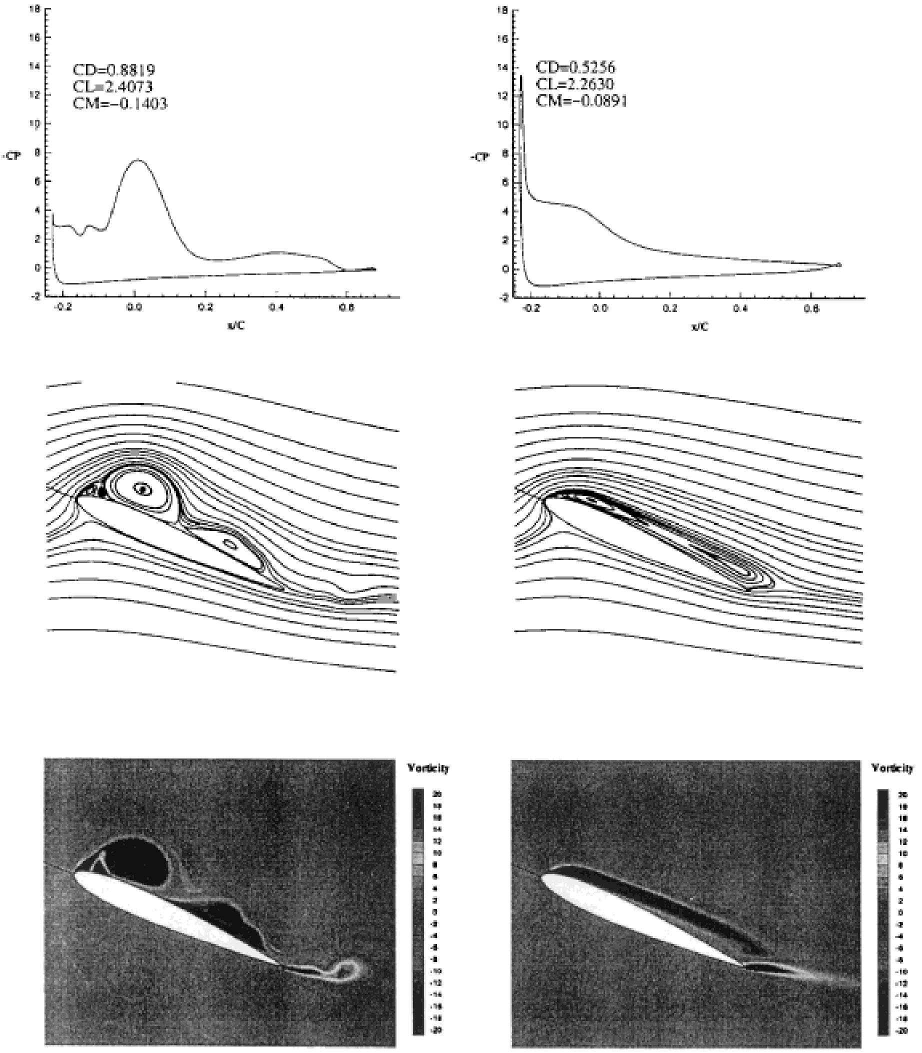

Figure 2 (*continued*)

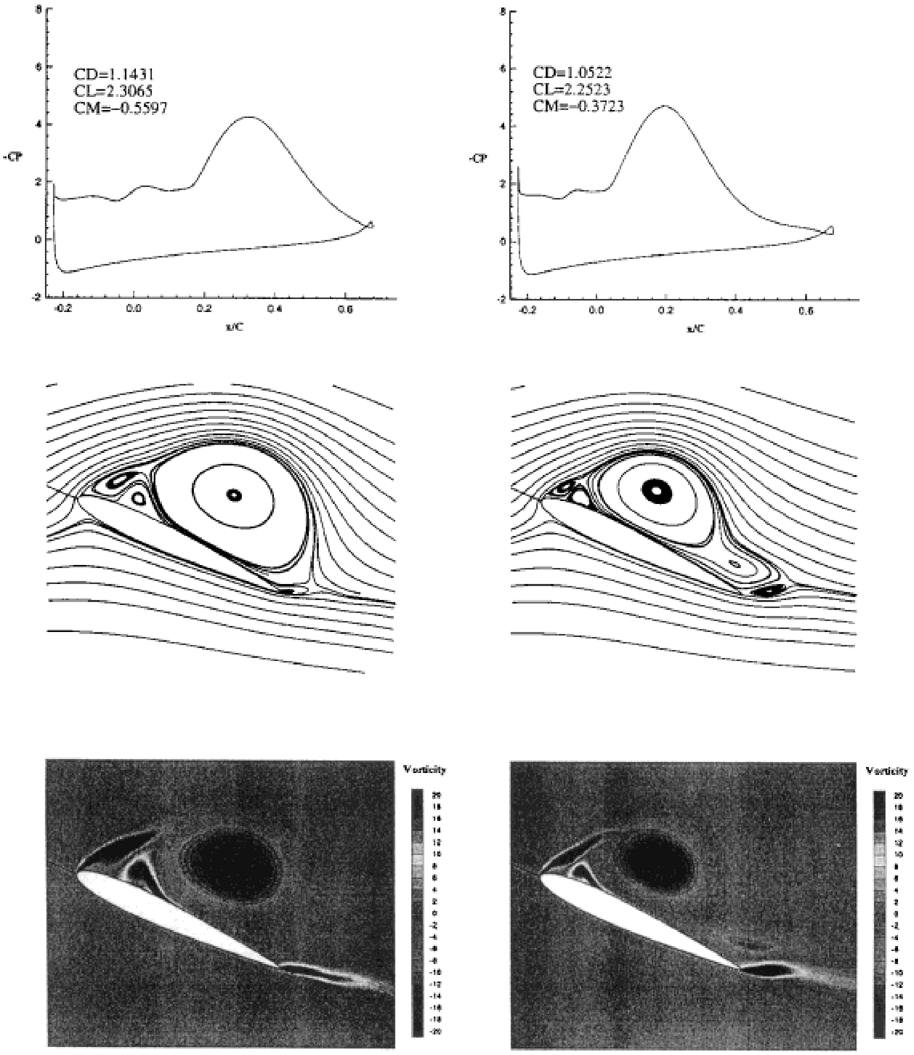

2h) α=25.0 deg

Figure 2 (*continued*)

2 i) α=24.9 deg down

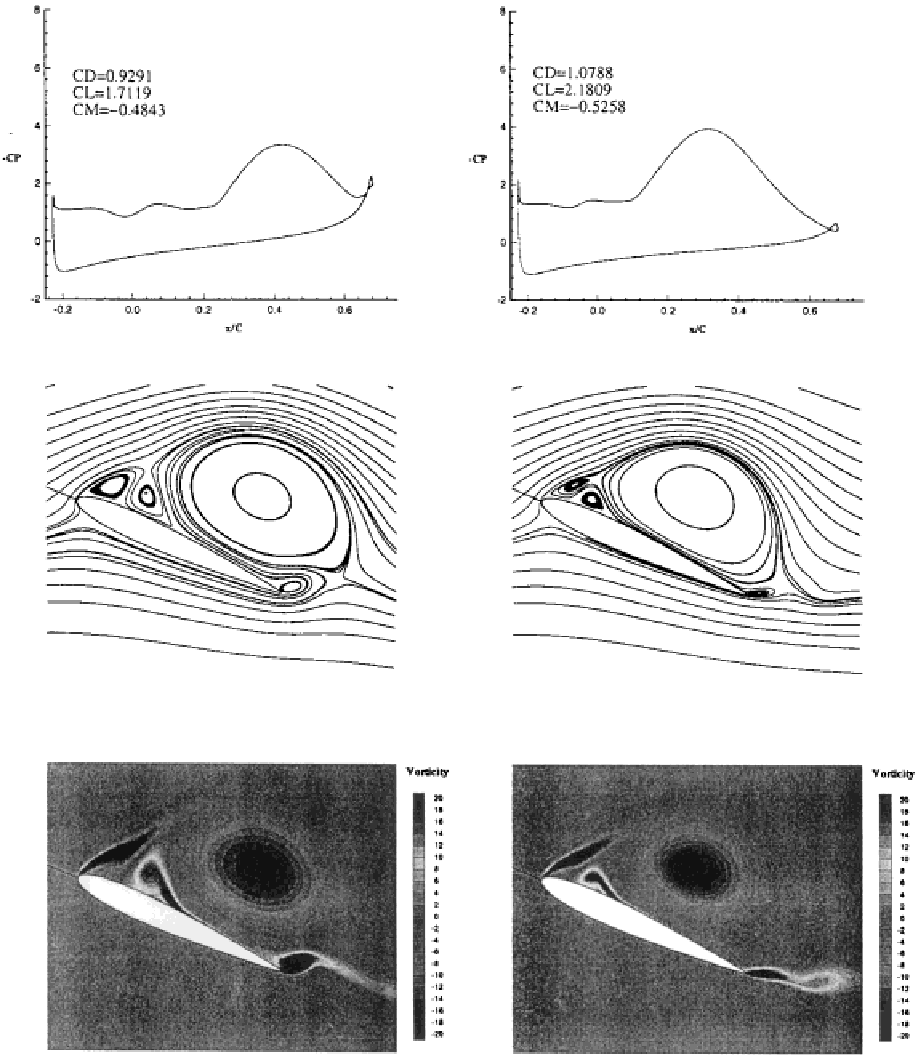

Figure 2 (*continued*)

2 j) α=24.5 deg down

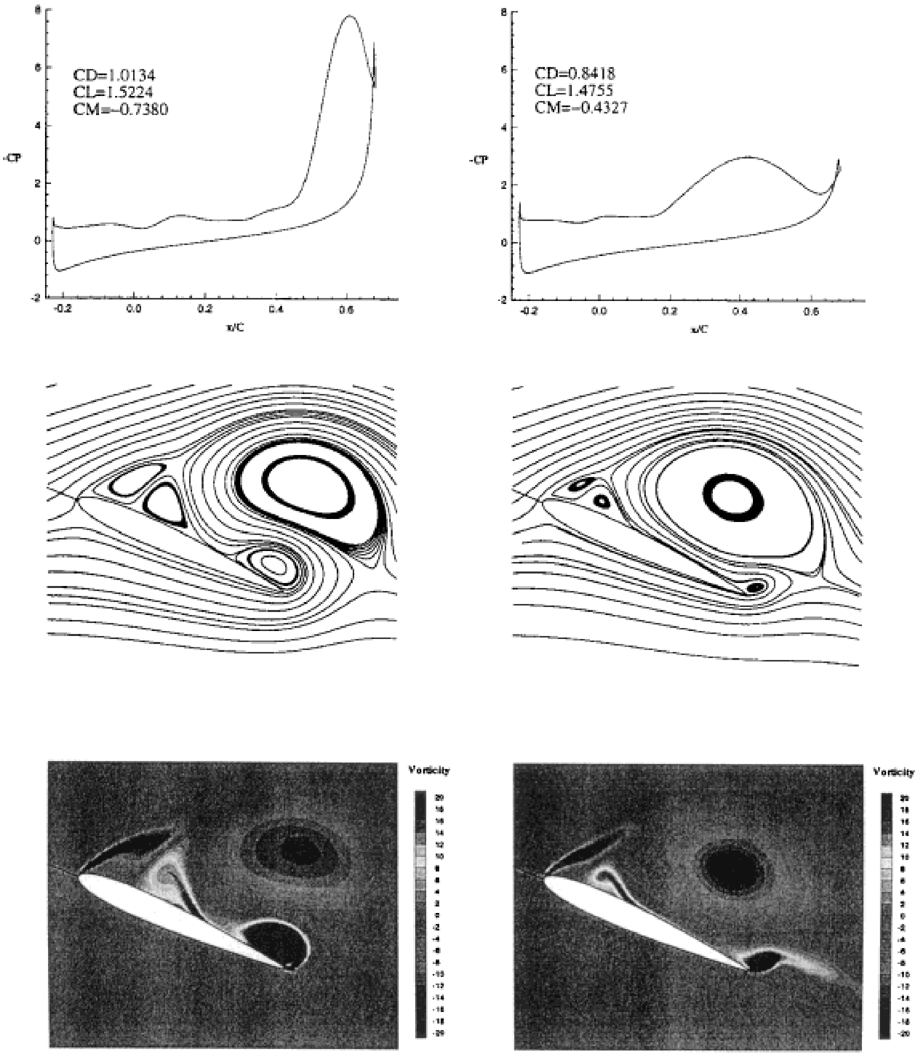

Figure 2 (*continued*)

2k) α=24.0 deg down

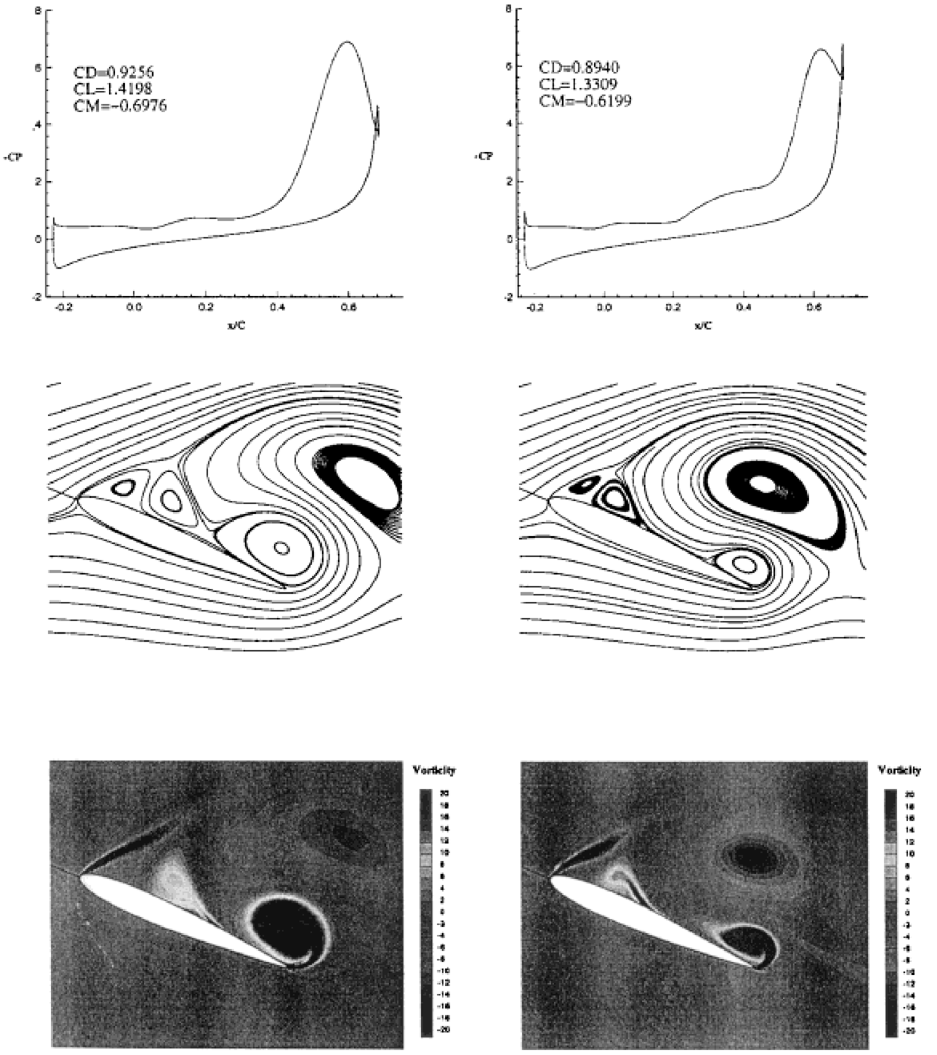

Figure 2 (*continued*)

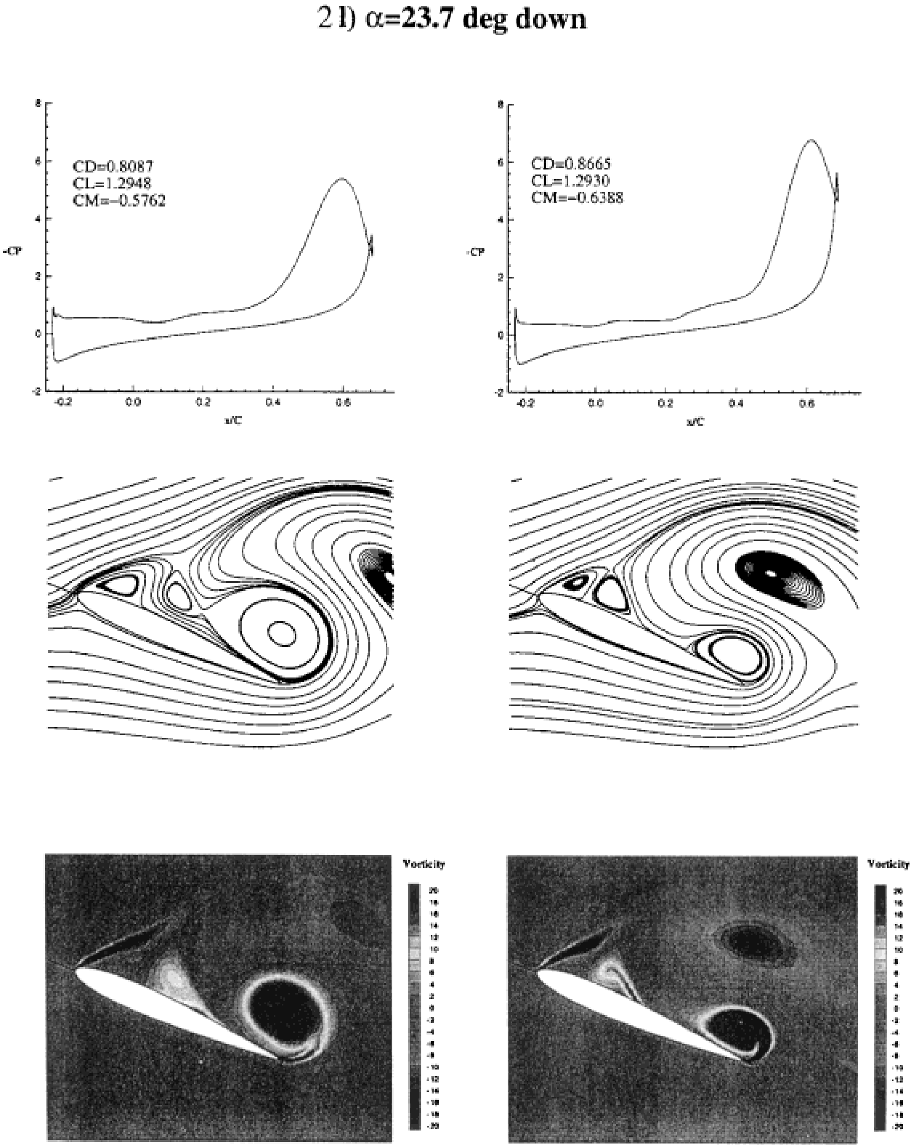
2 l) α=23.7 deg down

Figure 2 (*continued*)

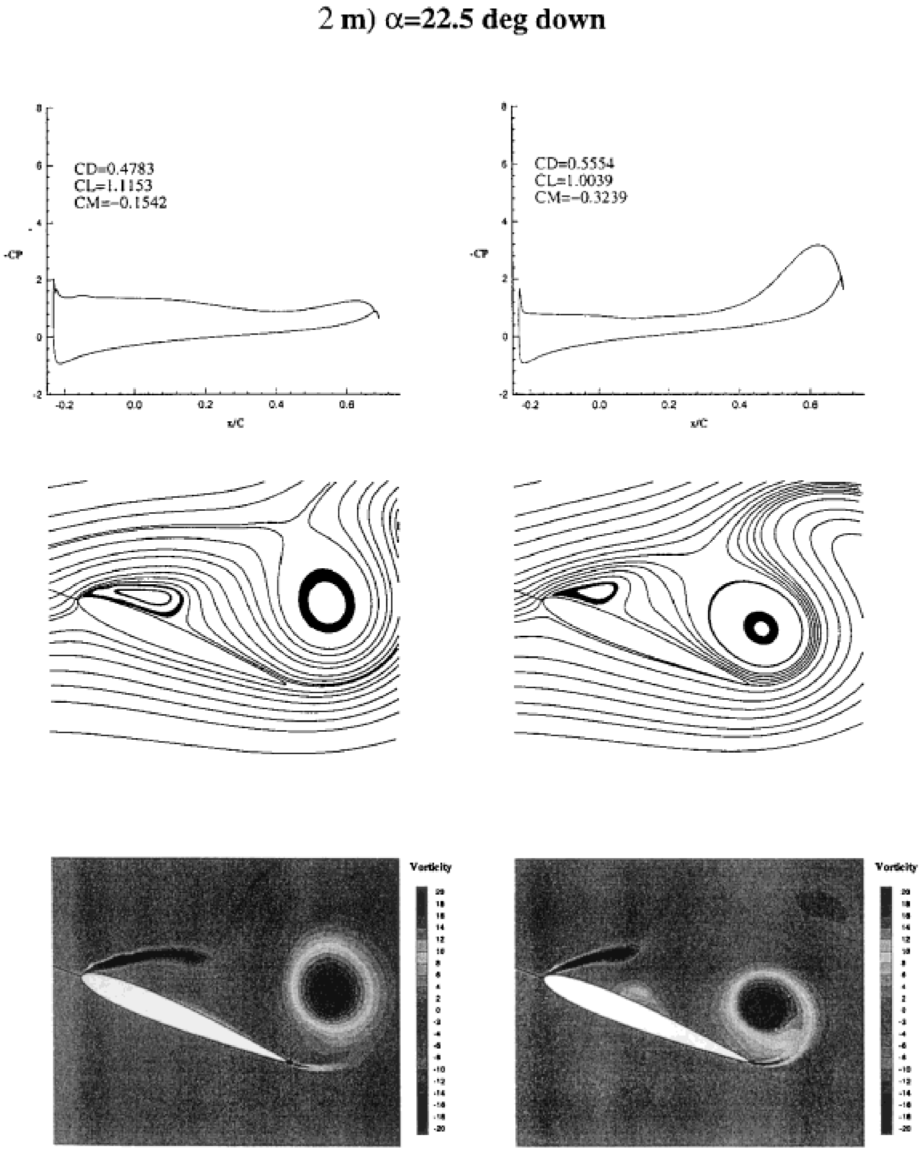

2 m) α=22.5 deg down

Figure 2 (*continued*)

2n) α=20.5 deg down

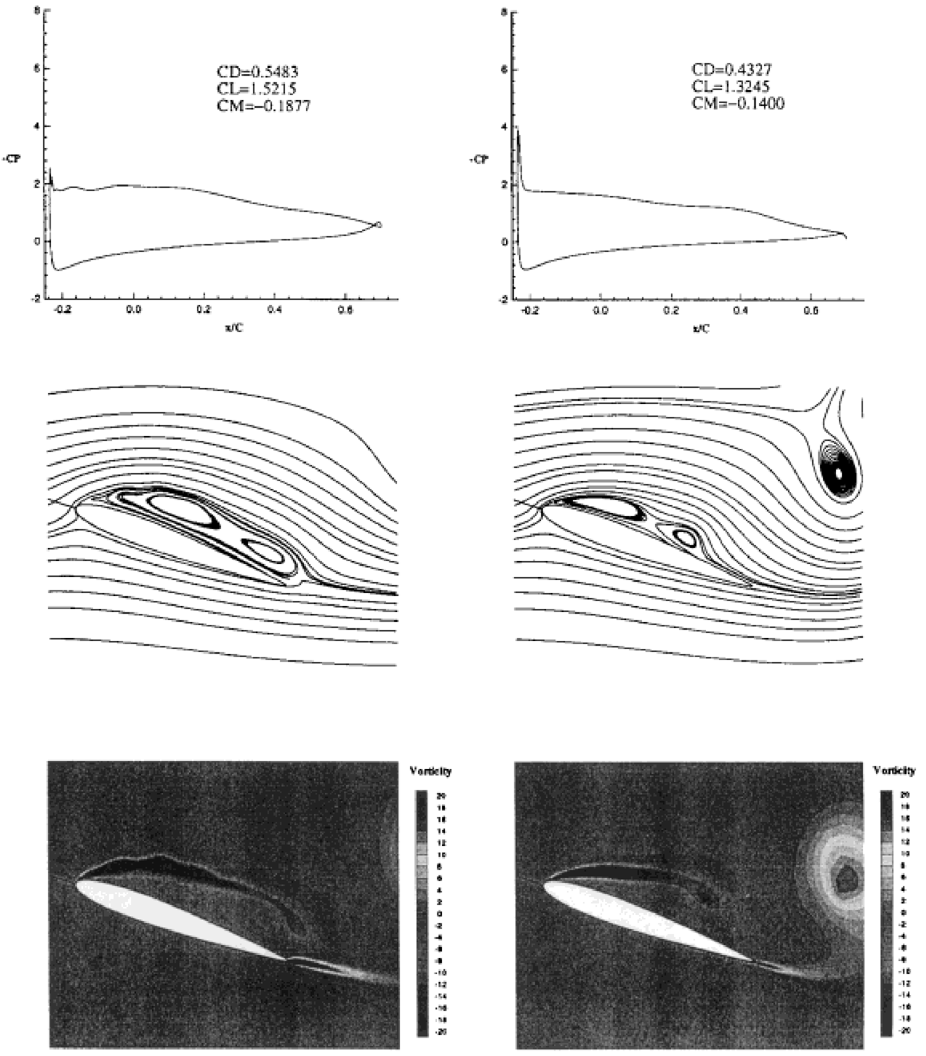

Figure 2 (*continued*)

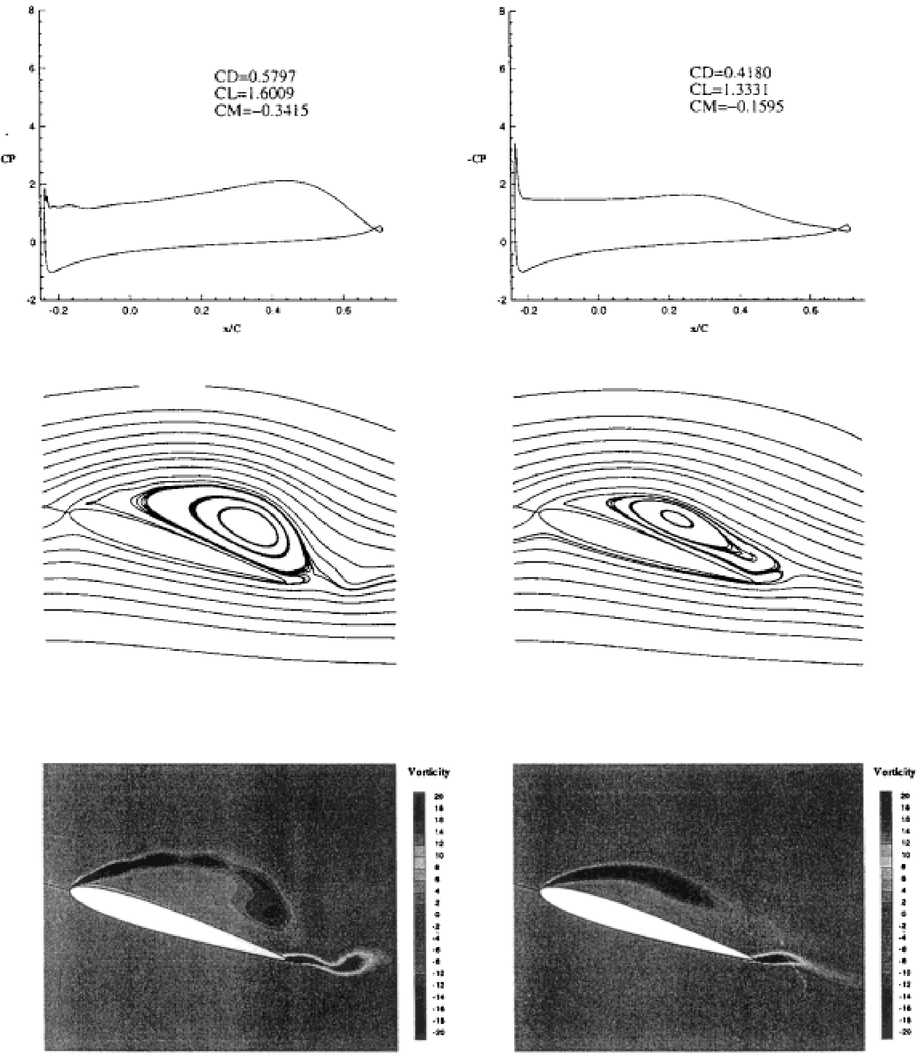

2 o) α=18.3 deg down

Figure 2 (*continued*)

2 p) α=16 deg down

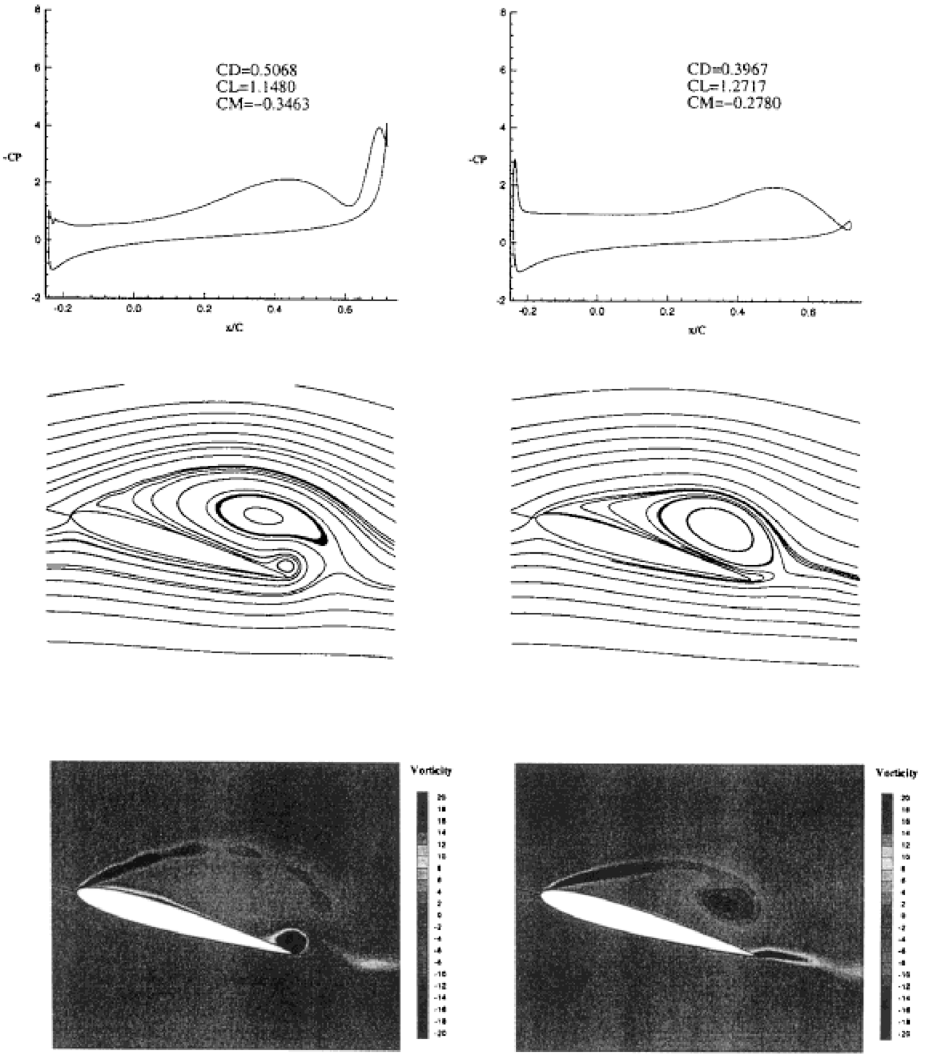

Figure 2 (*continued*)

2q) α=13.6 deg down

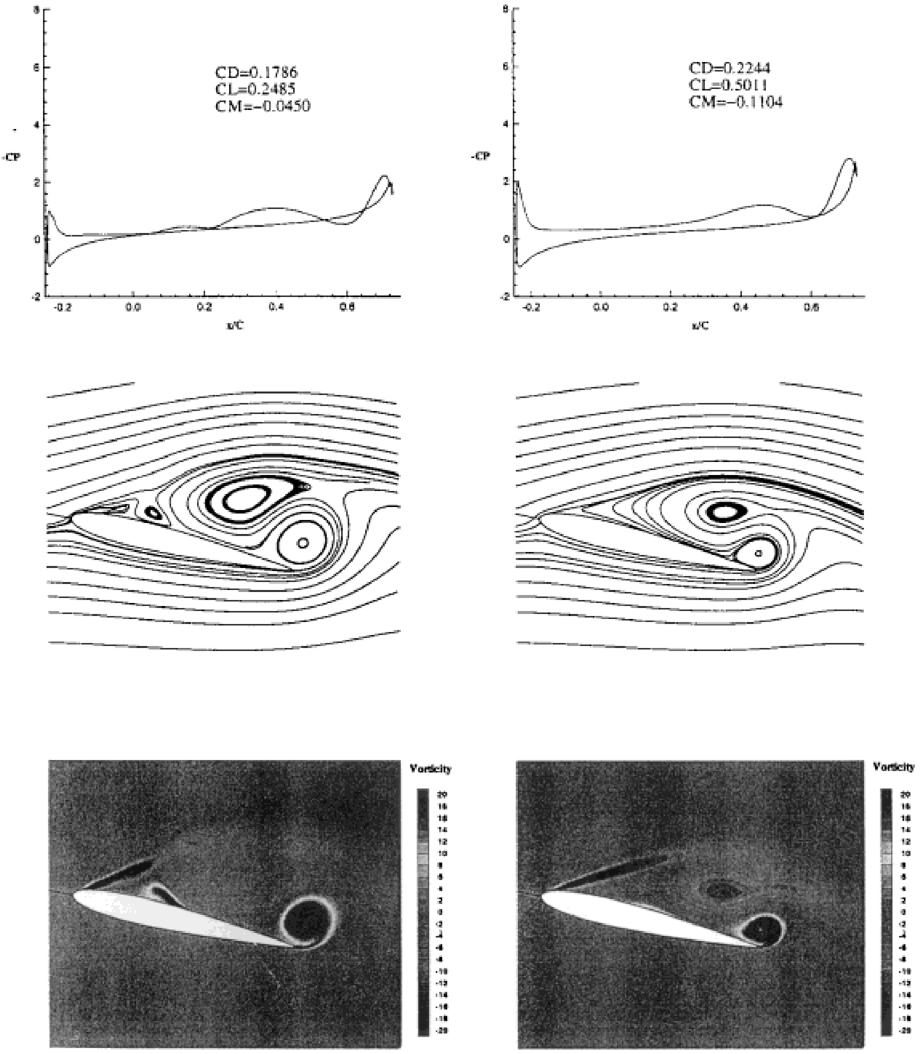

Figure 2 (*continued*)

2 r) α=11.3 deg down

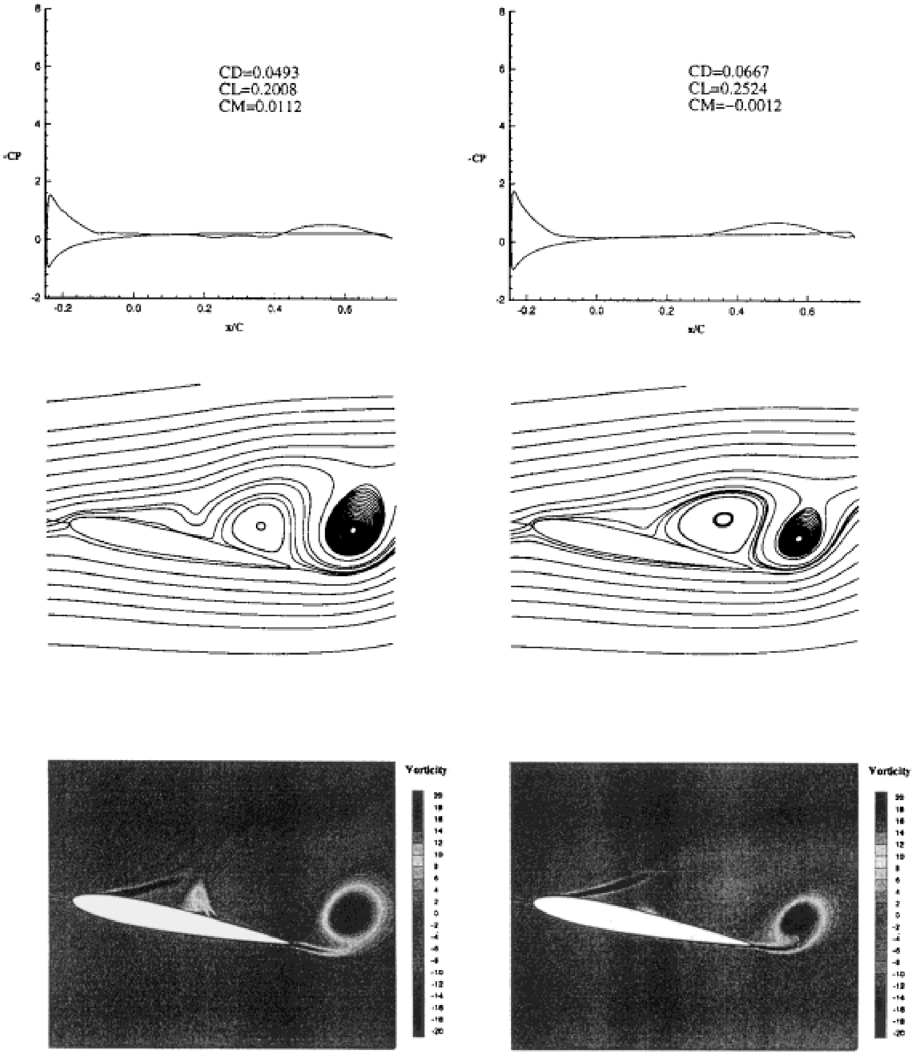

Figure 2 (*continued*)

2s) α=9.1 deg down

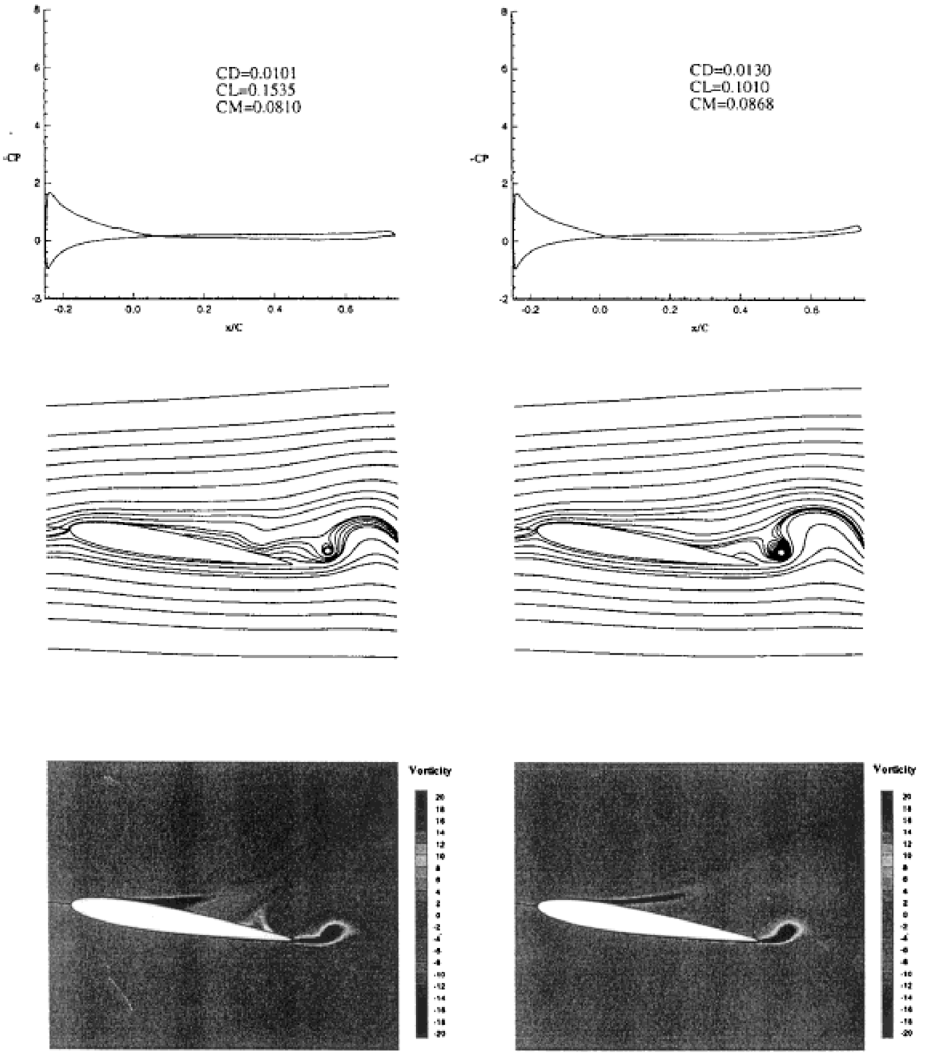

Figure 2 (*continued*)

2 t) α=7.4 deg down

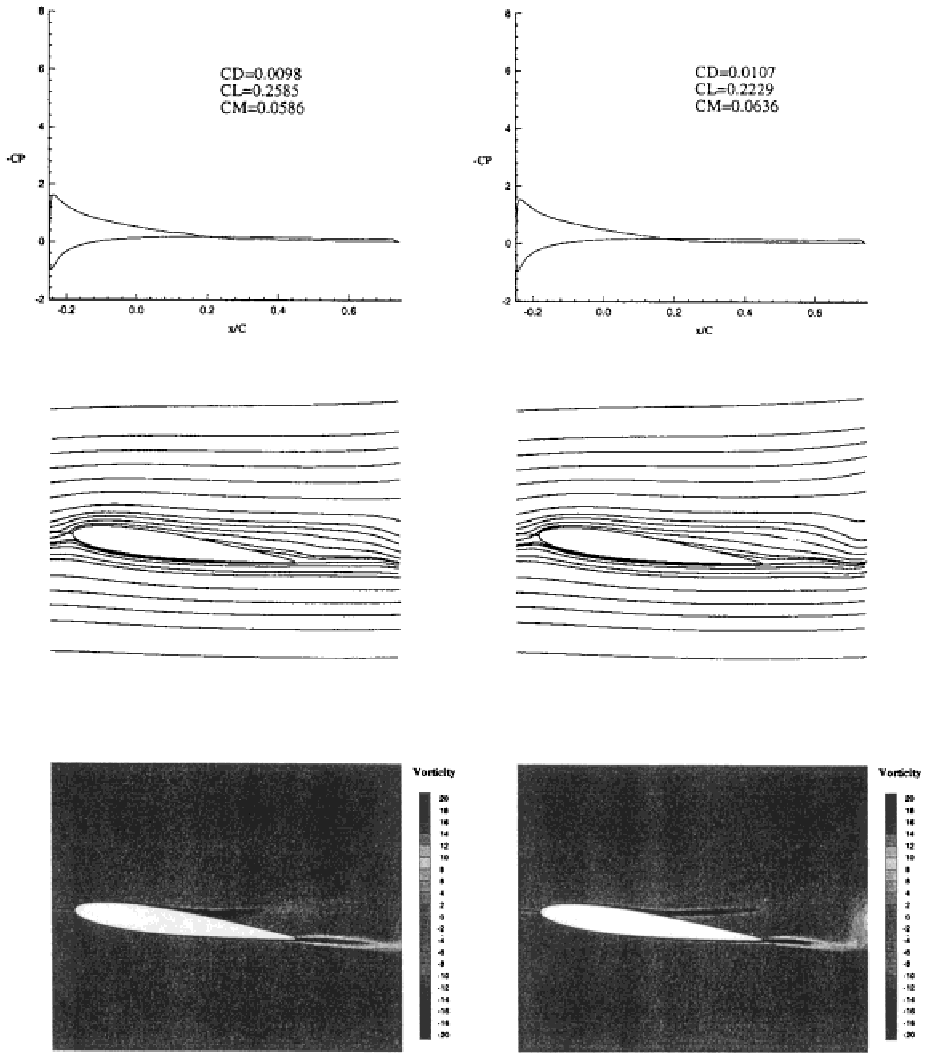

Figure 2 (*continued*)

2u) α=5.0 deg down

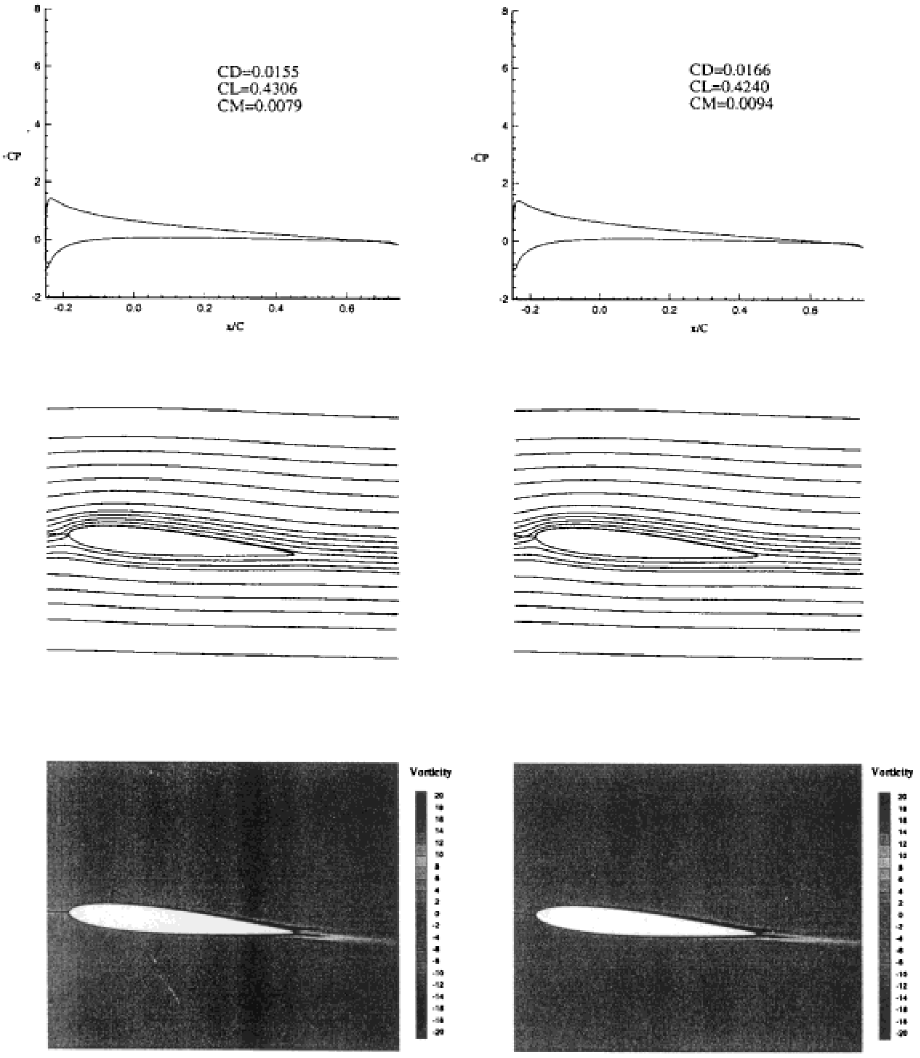

Figure 2 (*continued*)

model than with the BB model. This DSV is well known to be responsible for higher lift forces than those occurring at fixed incidence. At $\alpha = 24{\cdot}2^\circ$ the DSV is double-structured in both calculations, although twin eddies have already developed near the leading edge (Figure 2(g)). Also, the pressure found at this incidence with K–ω is very similar in shape to that found in Reference 36 at 23·6° (see Figure 3). Streamline data[35] indicate also a multiple-eddy structure at 24° with a high-vorticity region emanating from the leading edge. This is confirmed by the formation of the leading edge vortex found in Reference 36 at $\alpha = 23{\cdot}2^\circ$. Thus, during this upstroke phase, streamlines seem to be better described by the BB model than by the K–ω model. Levels of vorticity peak at about -22 in both calculations, slightly lower than the experimental maxima[35] found, about -24. During the final part of the upstroke the rate of increase in the DSV is more pronounced near the trailing edge than near the leading edge. At the maximum incidence (Figure 2(h)) the velocity field changes drastically: the DSV separates from the aerofoil near the leading edge, while the low pressure level at about 79 per cent chord pulls fluid with anticlockwise vorticity from the pressure surface, causing the formation of a small trailing edge vortex (TEV) as α takes its maximum value. This TEV has been noticed also in Reference 36 for the same pitching motion but at $Re = 44{,}000$; it contributes, while growing as here, to lifting the DSV from the upper aerofoil surface. However, while the DSV dwells on the suction surface over a large part of the oscillation cycle, the TEV takes place within a much smaller fraction of the cycle but its growth provokes a large oscillation in the lift coefficient. Again the level of vorticity maxima in the leading edge shear layer is about 22, in rather good agreement with the data.[35] However, Raffel *et al.*[35] indicate a vortex shedding from the leading edge region which is not captured by the tested turbulence models, as well as a strong variability of the DSV from cycle to cycle which is not found in the experiments. This could be a Reynolds number effect, but it indicates more likely the incapacity of statistical models to capture the randomness of the flow, which is one of the most dominant experimental features of the downstroke phase. This fact was already mentioned in References 35–38.

In contrast, the flow features during the beginning of the downstroke are very similar in both models and the extent of the recirculation zone is significantly higher than in the experiments at $\alpha = 24{\cdot}5^\circ$ and 24° (Figures 2(j) and 2(k)). The DSV core passes off the trailing edge at 24·6° with the BB model and slightly later with the K–ω model; such values can be compared with the value of 24·8° found in Reference 36. The shedding of the DSV occurs between these incidences with the BB model and around 23·5° with the K–ω model, which seems slightly favoured by a comparison with the experimental data.[35] Such discrepancies between the models are fully consistent with the fact that the convection velocity of the vortex is slightly higher for the BB model (between 0·36 and 0·55) than for the K–ω model (between 0·3 and 0·4), in good agreement with the experimental data around 0·35–0·4 indicated in Reference 11. The TEV which has grown to a large vortex leaves the trailing edge at almost the same decreasing incidence as the DSV, in agreement with the experiments.[37] In the wake the DSV and the TEV combine to form a structure whose cross-section looks like a mushroom and which evolves, moves upwards and increases in size as it convects downstream. This structure is characteristics of vortex-shedding phenomena; it has also been evidenced in References 37 and 39 and could be significant in blade–vortex interactions and aerodynamic sound generation. The occurrence of a secondary vortex near the leading edge (LEV) and the associated increase in lift during the downstroke motion which was noticed in Reference 40 is also found in the present calculations. The LEV is seen to emerge from the twin- eddy structure found near the leading edge at $\alpha_{\max}$ and contributes to the lift coefficient, which is found to increase by about 50 per cent and 30 per cent between 22·5° and 20·5° (Figures 2(m) and 2(n)), while the LEV extends along the suction side of the aerofoil. Its intensity is rather low, as indicated by the very weak leading edge suction peak. When the incidence is decreased further, the LEV extends along the whole chord while moving downstream (Figures 2(o)–2(s)). The reattachment of the flow starts from the leading edge at about

13° and occupies 60 per cent of the chord at 7·4°, in good agreement with the data.[35] Also, experimental data[36] indicate a complete reattachment at about 7°, slightly sooner than in both calculations (Figures 2(t) and 2(u)).

It is interesting to compare the computed wall pressure coefficients with the measured ones (Figure 3). The agreement between the two is very satisfactory during the upstroke phase. The maximum pressure peak is computed at about 16·8, whereas it is measured at 13·5; thus the intensity of the low pressure associated with the DSV core is strongly overestimated, especially with the BB model. Also, as usual, the experimental data lead the computed ones. Finally, the downstroke phase no longer sees the influence of the shed vortices for incidences lower than 20°.

Hysteresis loops are presented in Figure 4. Similar trends are found with both models during the upstroke phase, which shows a lift slope in good agreement with the experimental data and with the lift slope of the corresponding steady flow. However, the BB model is seen to slightly underpredict the stall angle (defined as the point of maximum C_L) at 23·8° if the flow is computed as fully turbulent, with a correct prediction at 24·4° with a transition point arbitrarily located at the pressure peak. The K–ω model yields in contrast a correct stall angle which is not influenced by a transition point imposed at the pressure peak. The computed maximum lift coefficient is about 2·47 with the BB model and 2·26 with the K–ω model and in the experiments. At the maximum angle of attack the lift coefficient is found at 2·30 with the BB model and 2·25 with the K–ω model, somewhat higher than the value of 2 found in the experiments. This disagreement is, however, far weaker than that found in References 11 and 12. During the downstroke phase, differences between the models and the experimental data become more important. A first lift minimum is found at $\alpha = 23{\cdot}5°$ as an effect of the suction generated by the TEV. This minimum is found in both calculations but later at $\alpha = 22°$. The maximum lift is found in the experiments at about 1·2 for $\alpha = 19°$. Two minima are found with both models, with a general trend for the calculations to lag the experiments. The computed lift minimum is about 0·15 with the BB model and 0·10 with the K–ω model close to $\alpha = 9{\cdot}1°$, whereas the experiments find it at $\alpha = 4{\cdot}3°$ with a value close to zero.

The drag coefficient experiences a rapid increase during the upstroke, with a maximum value 10 per cent higher than the experimental value of about 1·0. While the BB model follows closely the experimental increase, the K–ω model lags the experimental data. However, the most significant differences are found with both models during the downstroke phase, with a trend to the overprediction of drag. The time history of the moment coefficient also follows the development of the flow closely. As the leading edge suction grows, the nose-down pitching moment increases slowly from a low constant value. Just as the DSV vortex is shed, the minimum moment coefficient is about $-0{\cdot}64$ at $\alpha = 23{\cdot}7°$ down with the K–ω model and $-0{\cdot}74$ at $\alpha = 24{\cdot}5°$ down with the BB model, compared with the experimental value of $-0{\cdot}45$ at $\alpha = 24{\cdot}9°$ down. This disagreement is due to the computed enhanced low pressure within the DSV core. The trailing edge formation causes an indentation along the return cycle at about 20° down. This indentation is also found in both calculations, but it is significantly deeper owing to a suction effect which is stronger than measured experimentally (and lagged). This trend is fully consistent with the corresponding overprediction of drag. Subsequently, the moment coefficient levels off as the incidence decreases. It is then driven to its maximum value of about 0·8 in both models and in the experiments as well, but at a computed incidence of 10°, slightly too high. At this point the flow terminates its reattachment along the extrados.

Case 2

The second test case has been studied only with the K–ω model owing to its general superiority in the foregoing test case, with the aim of investigating the effect of reduced frequency. The values of

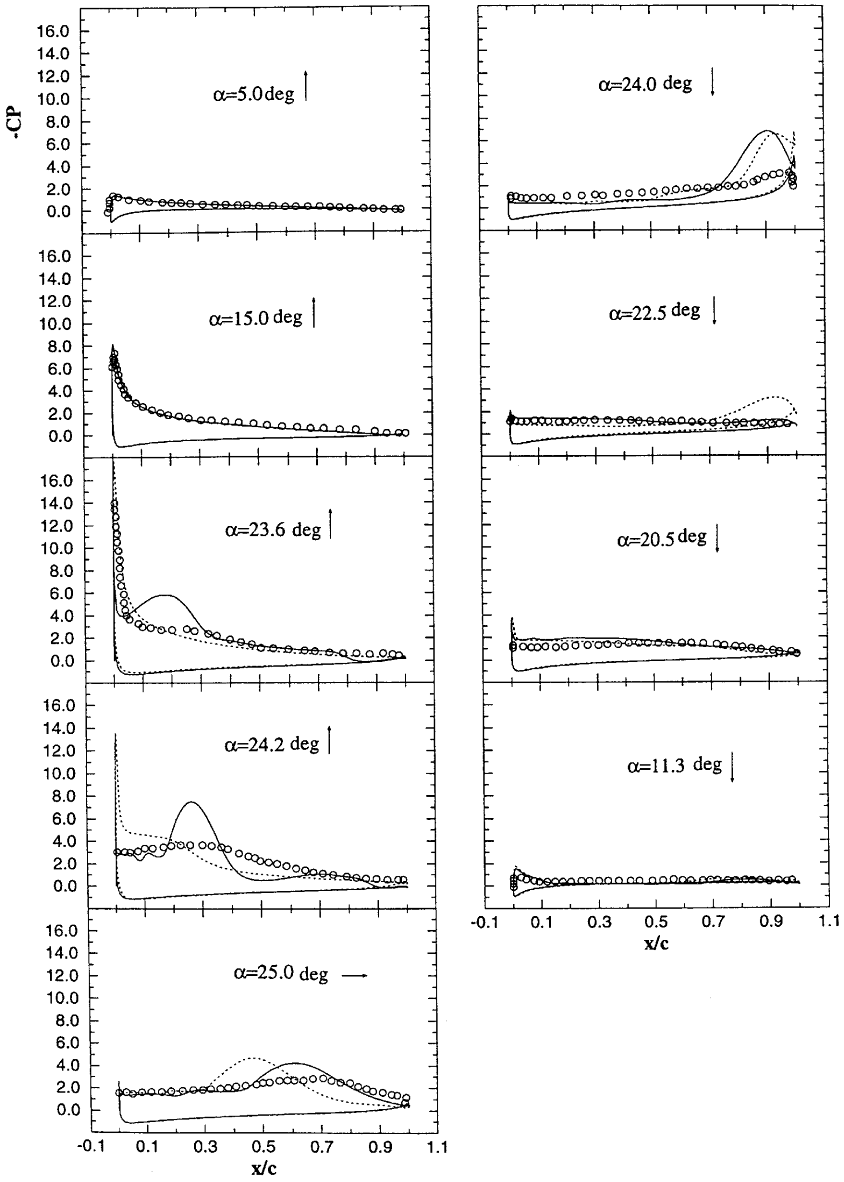

Figure 3. Flow past NACA 0012. $Re = 10^6$, $k = 0{\cdot}15$. Wall pressure coefficients: o, experimental data;[27] ····, *K–ω* SST model; ————, BB model

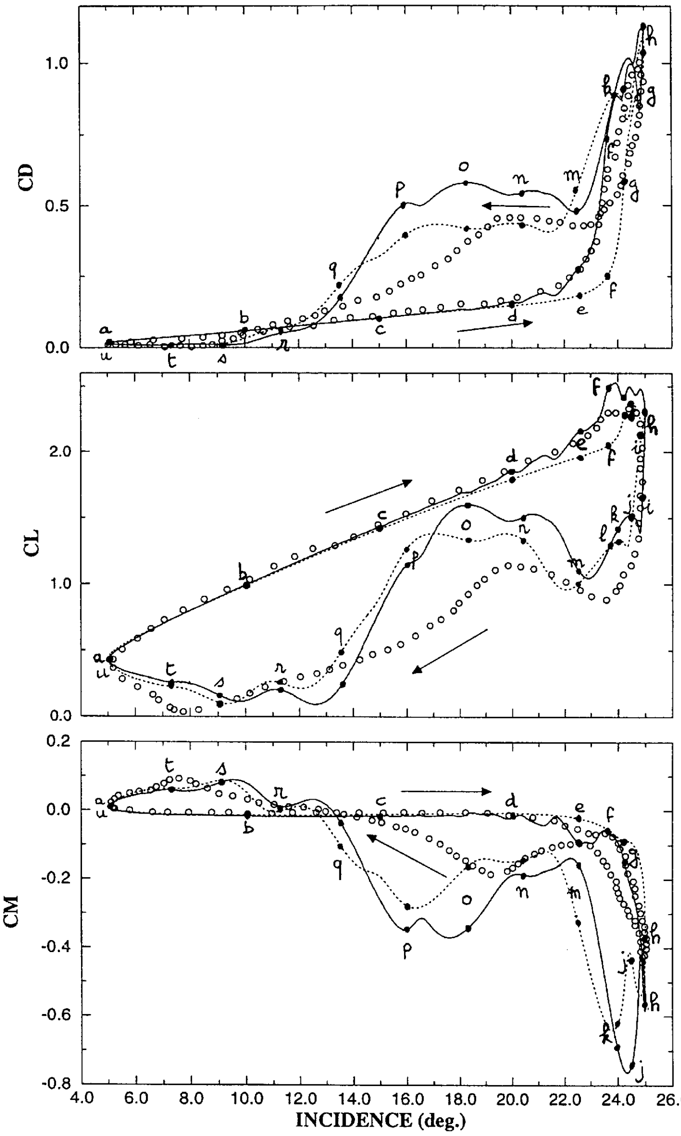

Figure 4. Flow past NACA 0012. $Re = 10^6$, $k = 0{\cdot}15$. Comparison between calculations performed with BB model and K–ω SST model. 200 × 90 O-type conformal grid. $\delta t^* = 0{\cdot}005$. Hysteresis loops of force coefficients. o, Experimental data;[27] · · · ·, K–ω SST model; ————, BB model. Time instants at which the flow has been plotted in Figure 2 are specified by a letter

the parameters are $\alpha_0 = 10°$, $\Delta\alpha = 15°$ and $k = 0{\cdot}10$. A time step $\Delta t^* = 0{\cdot}01$ (which does not yield force loops different from those resulting from $\Delta t^* = 0{\cdot}005$) is used, so that one cycle is represented by 3142 time steps.

The flow remains attached (Figure 5(a)) until a slightly lower incidence than for the previous case, around 15°, i.e. significantly higher than the 8° incidence observed in Reference 37 at a much lower Reynolds number ($Re = 44{,}000$). The upstroke phase is in good agreement with the experimental data, but for $\alpha > 20°$ some differences occur (Figure 5(b)). The development and expansion of the DSV show a lift stall which is slightly postponed with respect to the experiments, in which it occurs between 23° and 24°, just before the moment stall at 24°. Such a phenomenon is probably associated with the fact that a transition may occur in the experimental data in the suction peak zone. The main effect of a transition zone is to anticipate the development of the DSV during the upstroke phase, thereby improving the agreement with the experiments for lift and moment stall. Confirmation that the flow sequence evolves earlier than in the previous case can be evidenced: the streamlines at $\alpha = 24{\cdot}9°$ up (Figure 5(c)) resemble the streamlines at $\alpha = 24{\cdot}9°$ down (Figure 2(i)); also, the levels of vortex pressure minima and thus the DSV intensities are very similar, around -4. This could be expected, since the time elapsed until the aerofoil reaches its highest incidence is longer than in the previous case (because of the lower reduced frequency) when compared with the time taken by the aerofoil to complete the upstroke.

A postponed increase in lift and drag also follows the beginning of the downstroke (Figure 5(d)), but while the level of the drag is correct at about 0·9, the lift level is overestimated by about 70 per cent. This phenomenon is associated with the shedding of the DSV and the subsequent motion of the LEV downstream at about 22°, thereby leading to reattachment very quickly, around 16°, instead of less than 10° in the experiments. However, it is quite encouraging to see that the small anticlockwise loop around $\alpha = 25°$ found in the experiments[27] is reproduced (although too intensified because of the already noticed intensified lift level). The mentioned TEV is still present, although its effect seems less important because of the relatively low frequency, in correct agreement with Reference 37. A comparison of sequences of vortex shedding shows also a noticeable increase in the wavelength of vortices in the wake (see e.g. Figure 5(e)) when compared with the previous case. The most important differences are found in the lower branch of the hysteresis loop. However, some differences are not unexpected, as the lift loop is known to be sensitive to flow parameters other than k, e.g. surface roughness, aspect ratio, etc. The undulations of the lower branch have also been observed in the experimental data.[40] As in the previous case, the variations in the lower branch of the hysteresis loops (Figure 6) for C_L and C_M are due to the passage of the successive vortices following the DSV (Figure 5(f)).

Case 3

A third NACA 0012 test case has been performed with the following parameters: $\alpha_0 = 10°$, $\Delta\alpha = 15°$ and $k = 0{\cdot}25$. Except for the increased reduced frequency, the flow parameters are the same as in the previous case. The calculations show a reasonable prediction of the upstroke phase and of the beginning of the downstroke phase, with relatively well estimated maximum lift and drag. The effect of increasing the frequency is to delay the occurrence of the DSV, as indicated by a comparison between pressure coefficients at 24·9° for $k = 0{\cdot}1$ and 0·2 (Figure 7); this influence has already been noticed in Reference 40. It is also found that the lift increases until α_{max} and does not show significant hysteresis during the beginning of the downstroke, in contrast with the moment coefficient which stalls much later than the beginning of the downstroke. The DSV and the TEV appear to be shed together close to the maximum incidence as in Reference 37. However, the vortex-shedding instant is slightly postponed in the calculation, resulting in a delayed decrease in lift and drag, with

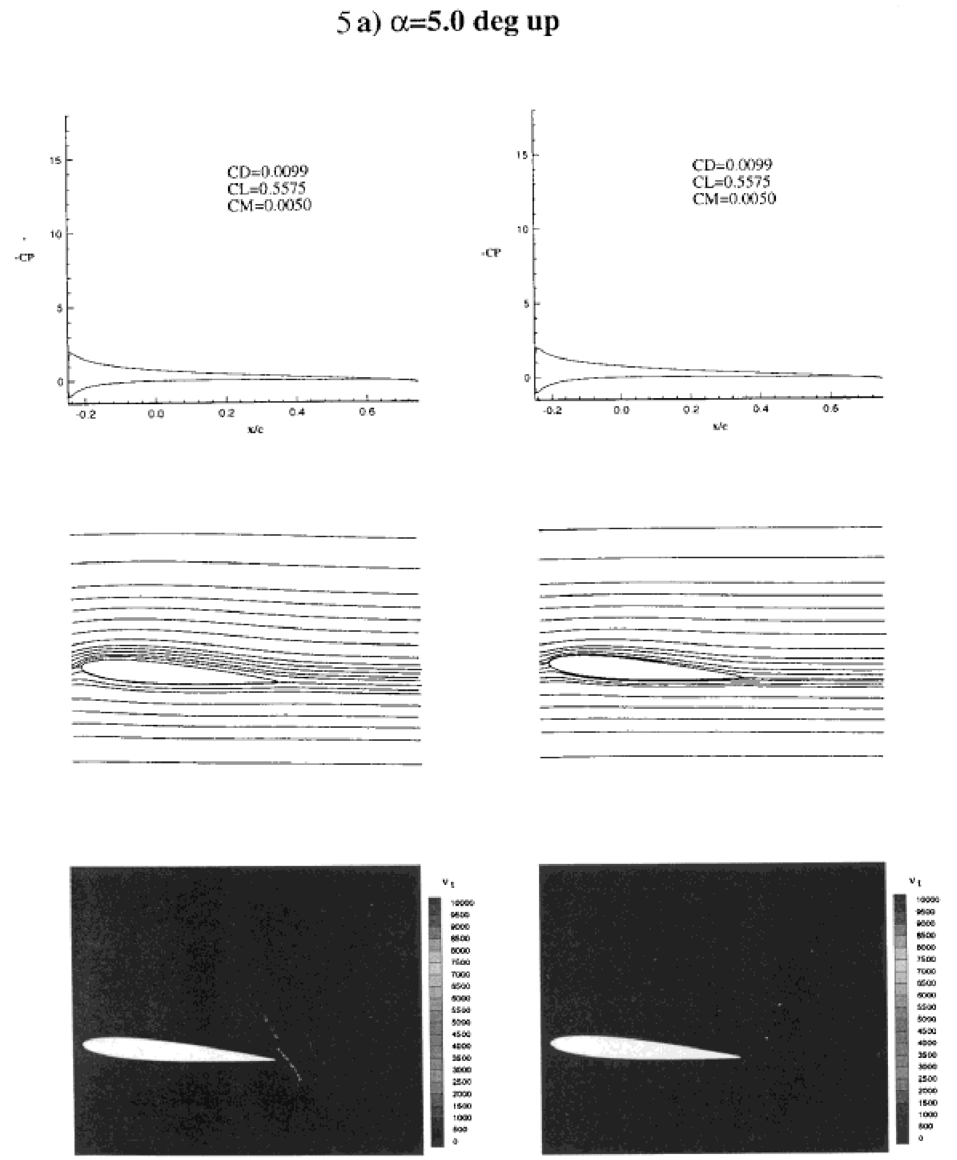
5 a) α=5.0 deg up

Figure 5(a)–5(g). Flow past NACA 0012. $Re = 10^6$, $k = 0{\cdot}10$. Calculations performed with K–ω SST model. 200 × 90 O-type conformal grid. $\delta t^* = 0{\cdot}01$. Left, fully turbulent calculation; right, transition near forward stagnation point. Time instants at which the flow is plotted in Figure 6 are specified by a letter

5 b) α=22.4 deg up

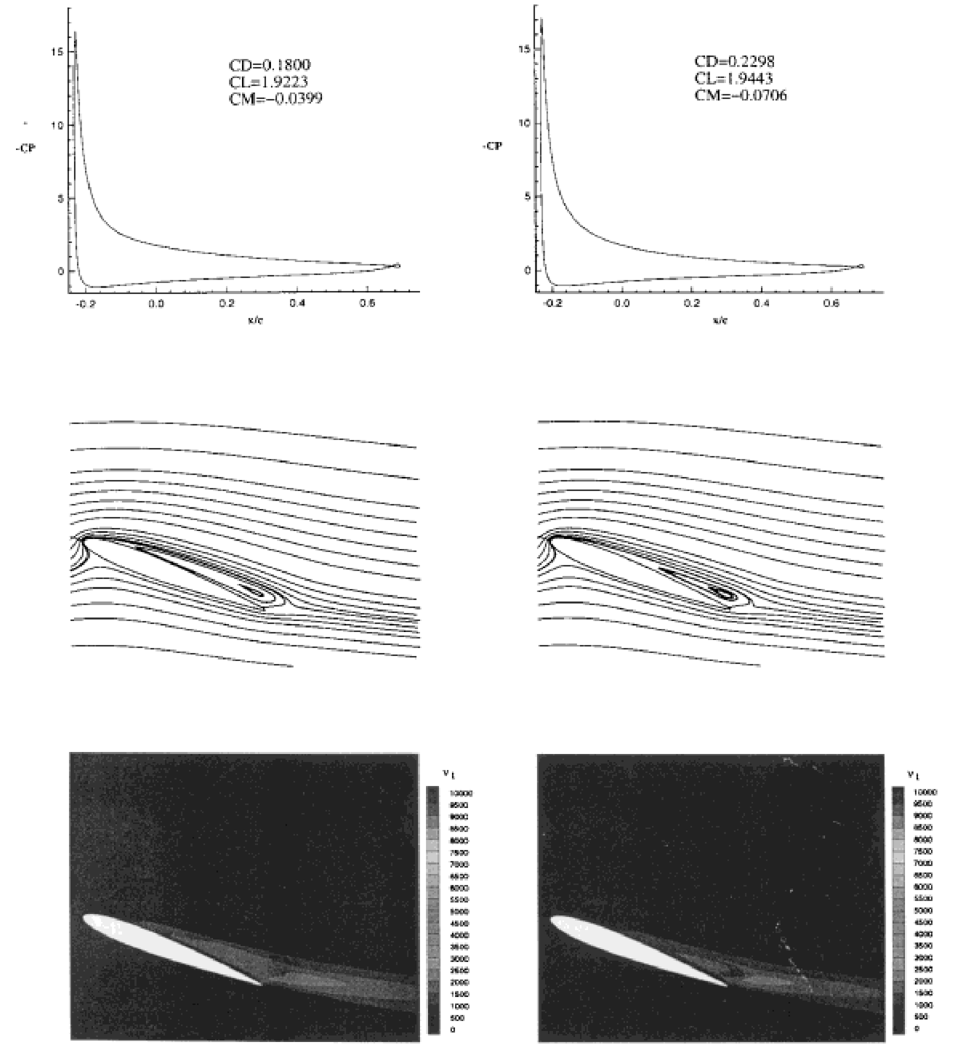

Figure 5 (*continued*)

5c) α=**24.9 deg up**

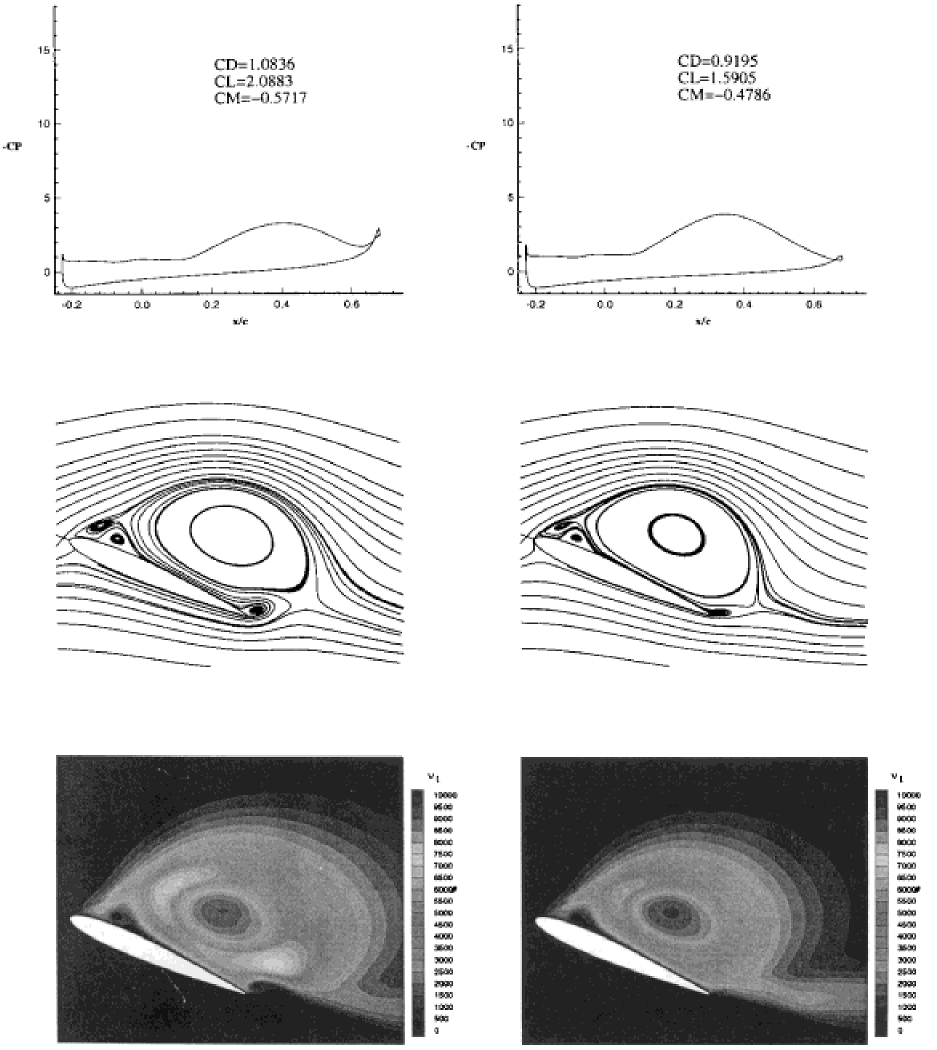

Figure 5 (*continued*)

5d) α=24.0 deg down

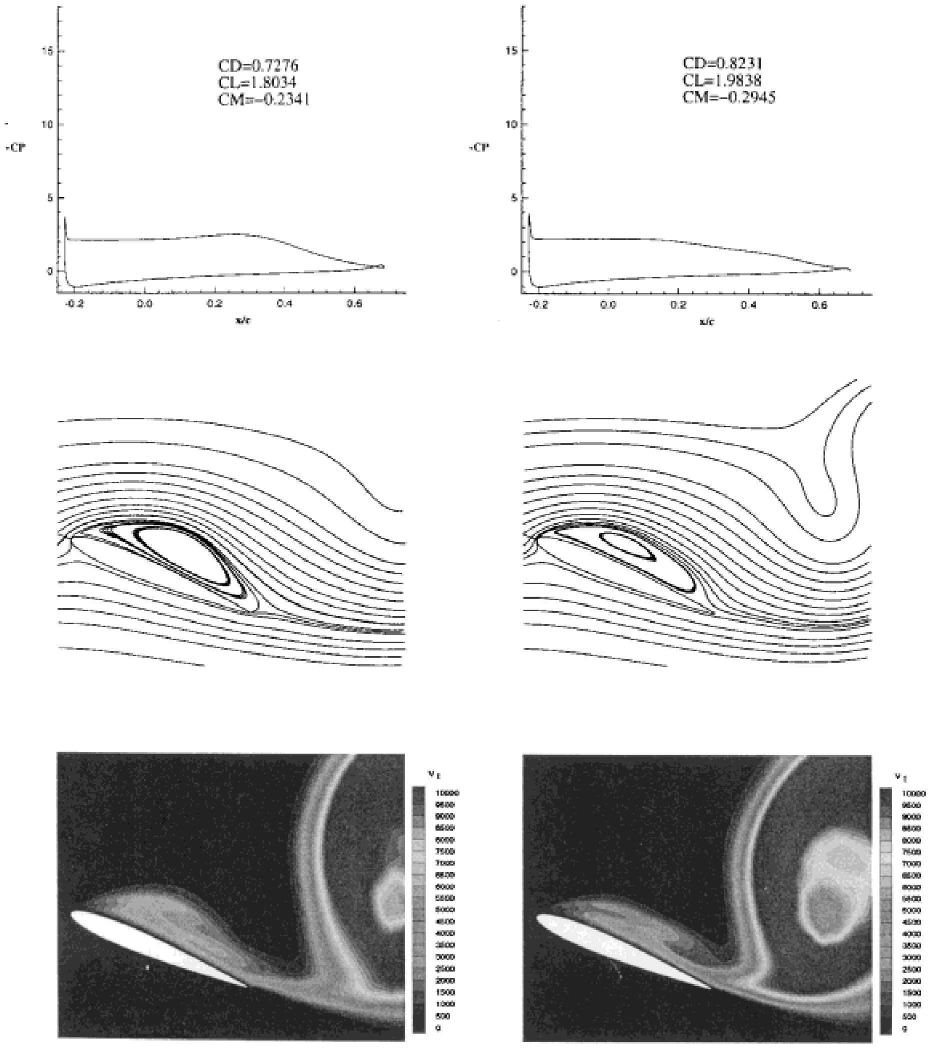

Figure 5 (*continued*)

5 e) α=19.9 deg down

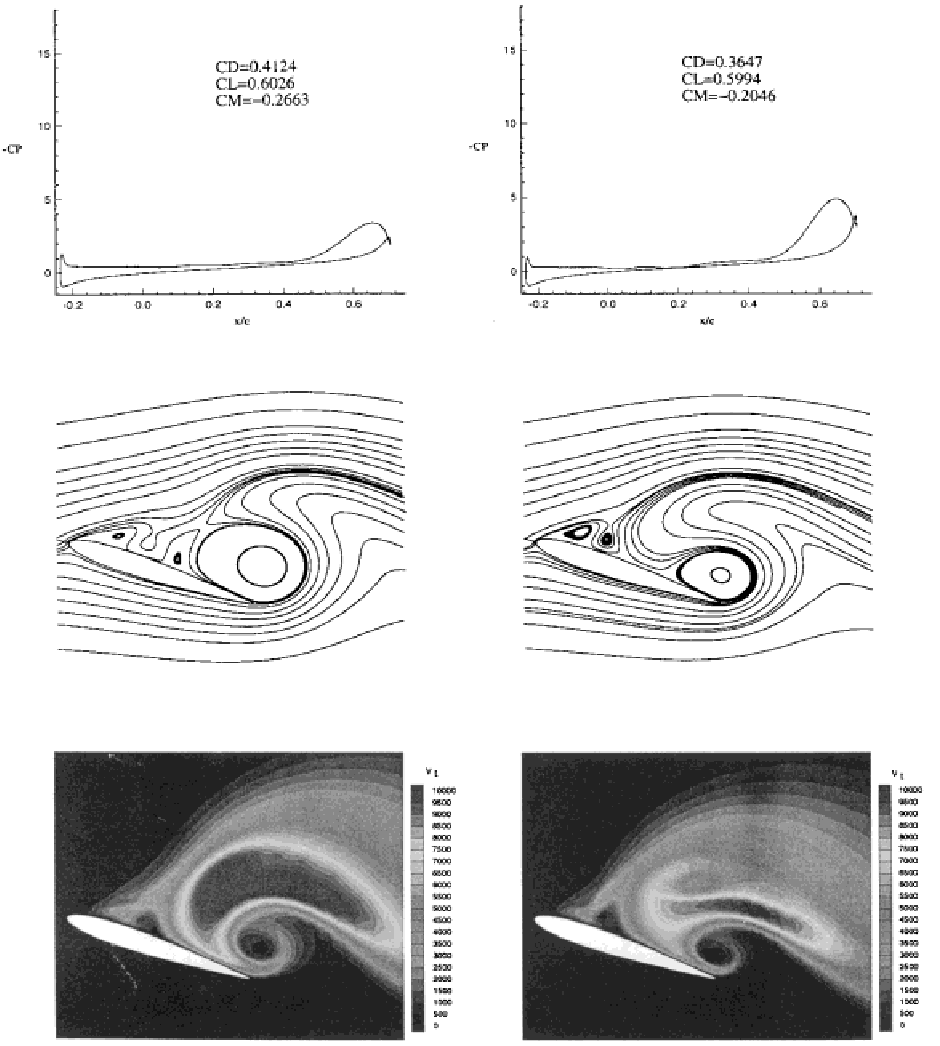

Figure 5 (*continued*)

5 f) α=14.1 deg down

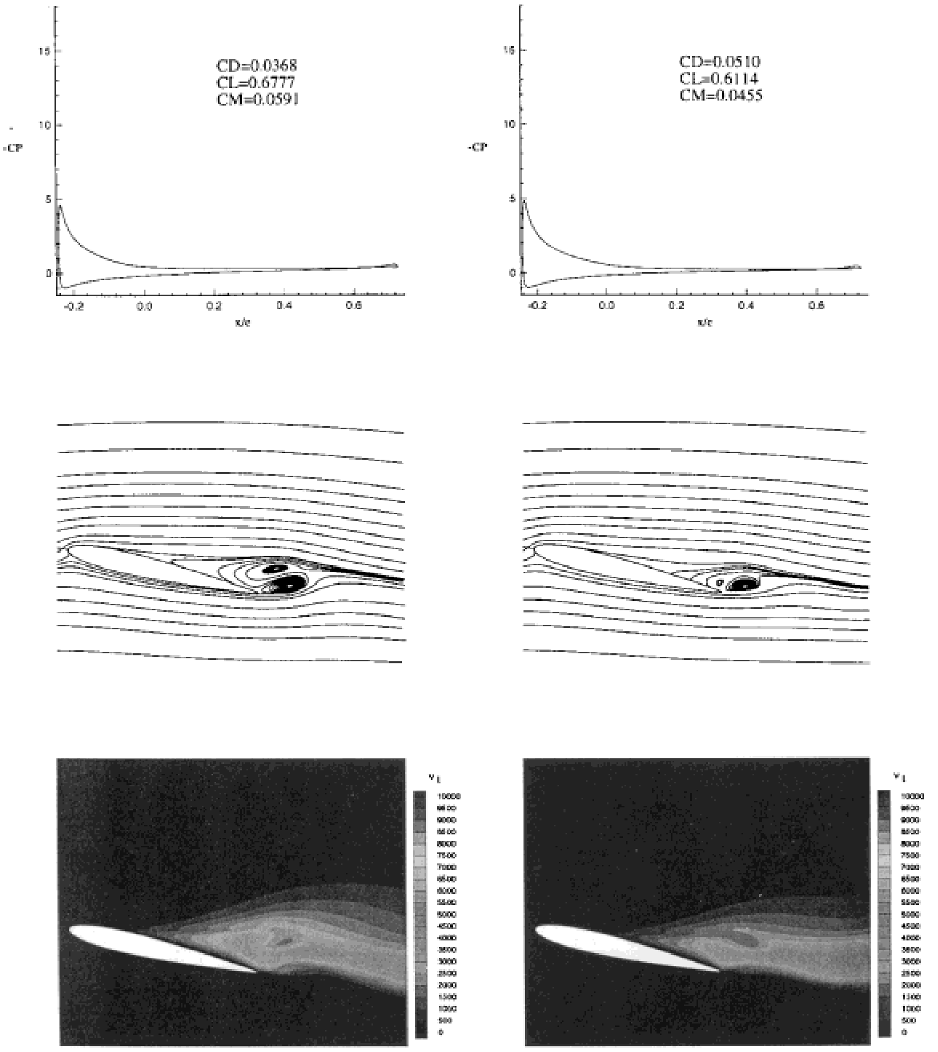

Figure 5 (*continued*)

5 g) α=8.6 deg down

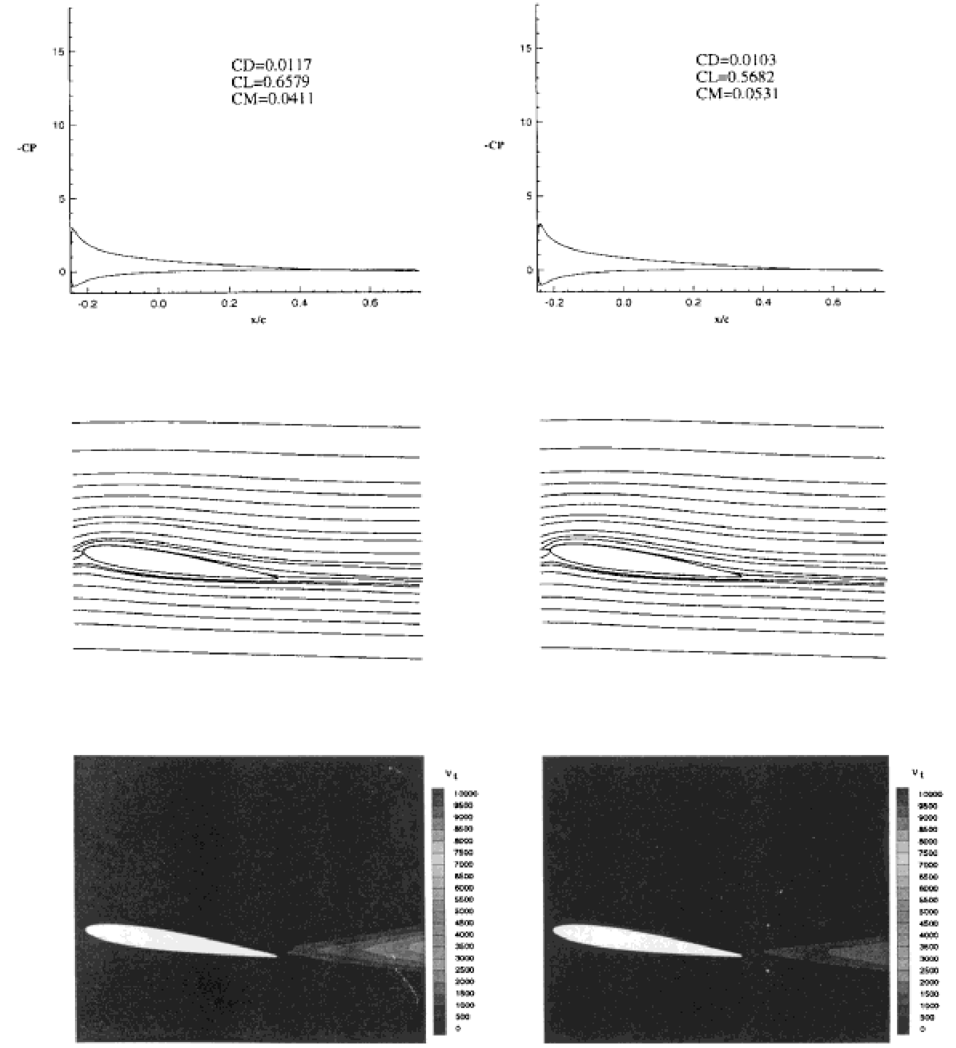

Figure 5 (*continued*)

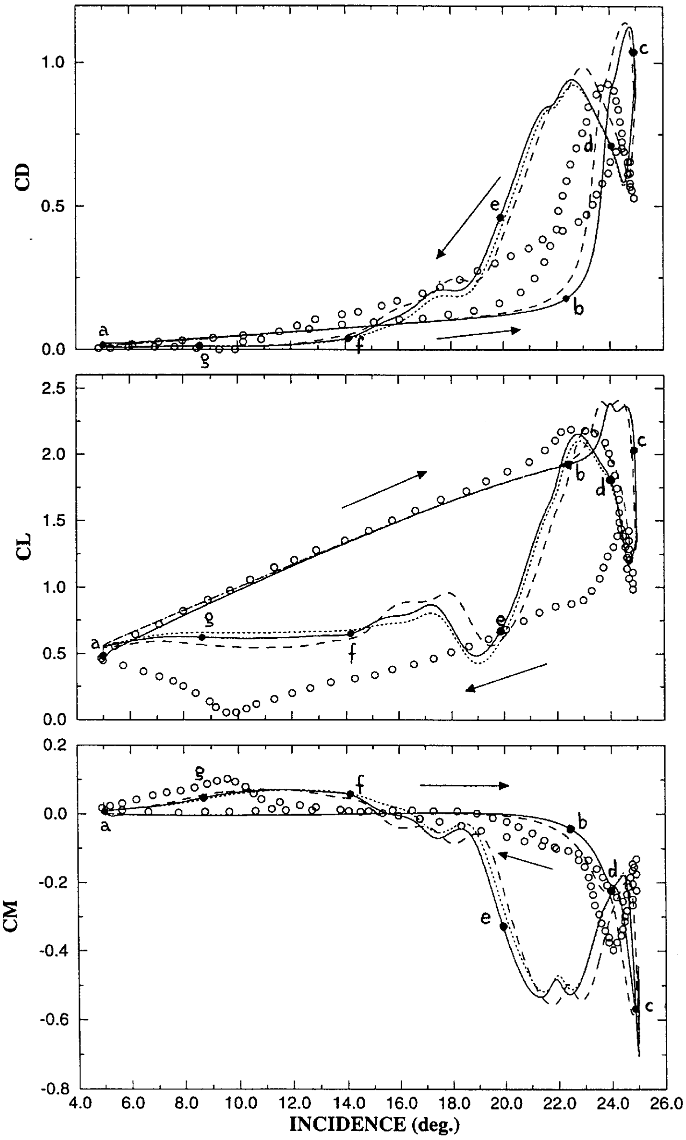

Figure 6. Flow past NACA 0012. $Re = 10^6$, $k = 0{\cdot}10$. Calculations performed with K–ω SST model. 200 × 90 O-type conformal grid. $\Delta t^* = 0{\cdot}01$; · · · ·, fully turbulent calculation, $\Delta t^* = 0{\cdot}01$ (up), 0·005 (down); — ———, transitional calculation, $\Delta t^* = 0{\cdot}01$. Time instants at which the flow has been plotted in Figure 5 are specified by a letter

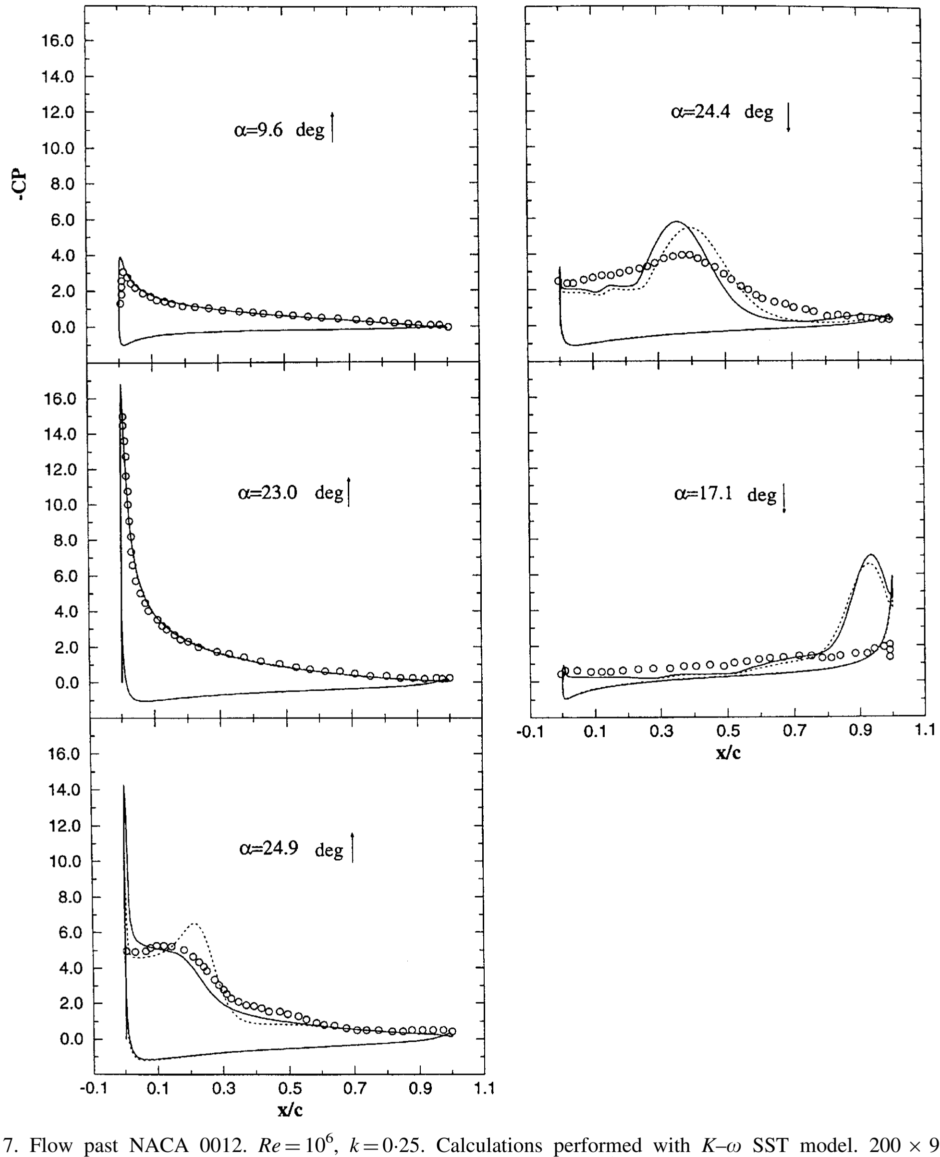

Figure 7. Flow past NACA 0012. $Re = 10^6$, $k = 0{\cdot}25$. Calculations performed with K–ω SST model. 200 × 90 O-type conformal grid. $\Delta t^* = 0{\cdot}005$. Wall pressure coefficients. o, Experimental data;[27] ····, transitional calculation; ————, fully turbulent calculation

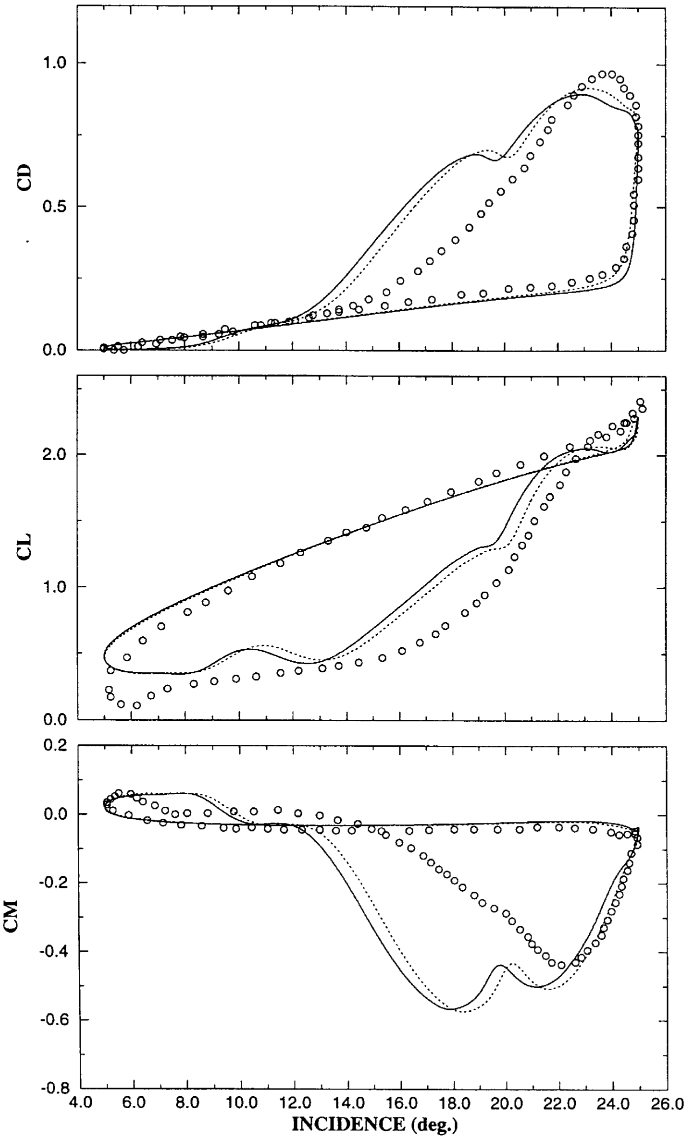

Figure 8. Flow past NACA 0012. $Re=10^6$, $k=0{\cdot}25$. Calculations performed with K–ω SST model. 200 × 90 O-type conformal grid. $\Delta t^*=0{\cdot}005$. Hysteresis loops of force coefficients. o, Experimental data;[27] ····, transitional calculation; ————, fully turbulent calculation

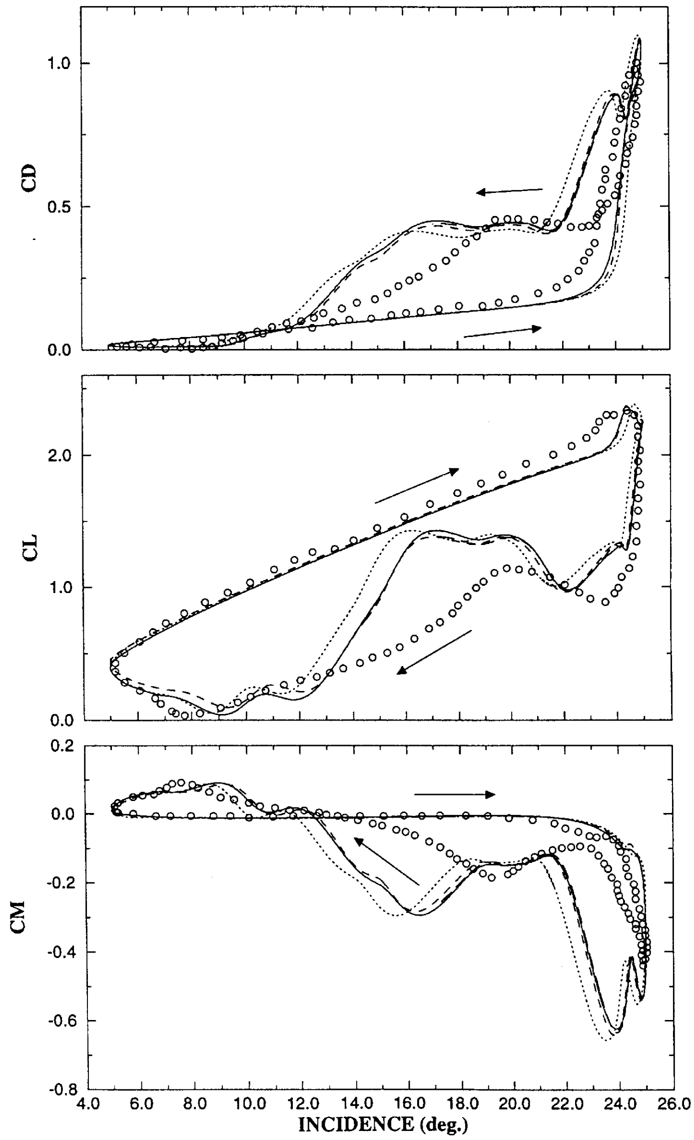

Figure 9. Influence of grid size and time step on force coefficients. $Re = 10^6$, $k = 0.15$. K– ω SST model. o, Experimental data;[27] —— –, 120 × 80 O-grid, $\Delta t^* = 0.01$; ····, 200 × 90 O-grid; $\Delta t^* = 0.01$; – ——, 200 × 90 O-grid, $\Delta t^* = 0.01$; — ———, 120 × 80 grid; $\Delta t^* = 0.002$

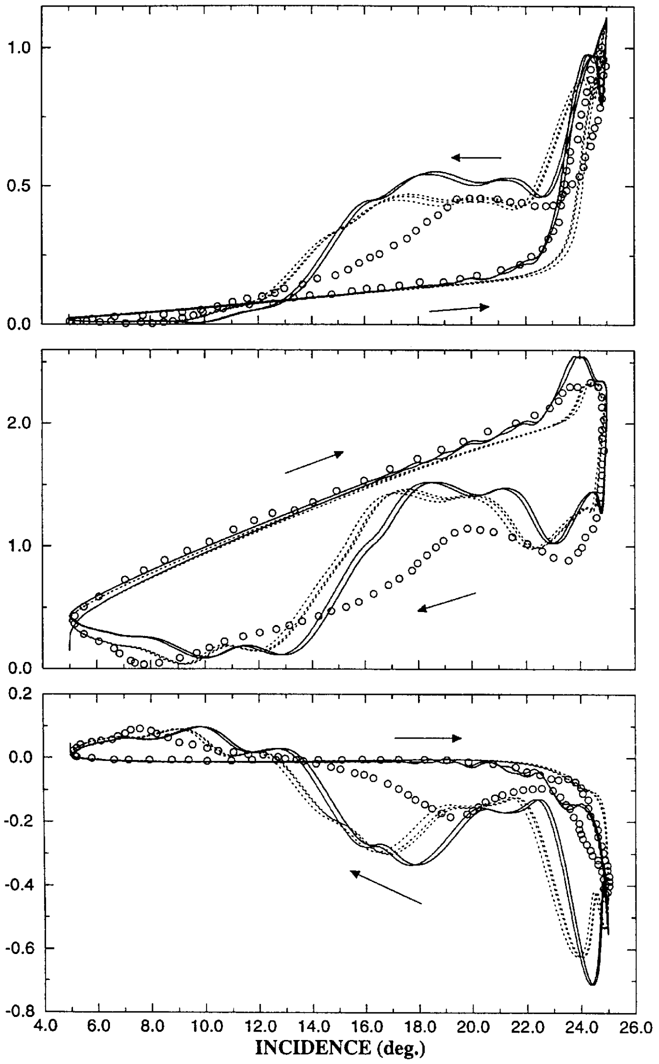

Figure 10. Comparison between force coefficients for cycles 1, 2 and 3 on 120 × 80 O-grid. $\Delta t^* = 0{\cdot}01$. ————, BB model; ····, K–ω SST model

significantly higher negative values of the moment coefficient. This is consistent with the presence of a high-suction region near the trailing edge, as shown by the wall pressure coefficient at $\alpha = 17{\cdot}1°$ down. In contrast, the wall pressure resulting from the experiments does not show any significant peak, indicating that the flow is still completely separated from the upper surface. The sweeping phase is achieved at about 8°, an incidence at which separation has been completely removed. The results also show that there is a slight improvement in global forces if the transition is imposed upstream of the suction peak (Figure 8), although previously mentioned trends during the downstroke are still present.

5. CONCLUSIONS

A new numerical method has been applied to the calculation of deep dynamic stall. Massive recirculation zones, the formation and convection of large vortical structures and the details of the dynamic stall phenomena have been identified and their relation to the reduced frequency has been assessed. The turbulence models used indicate good agreement with available data during the upstroke phase, in spite of significant differences which occur mainly during the downstroke phase. It is found that such differences are generated by the strong overestimation of the suction induced by shed vortices. This is probably due to the turbulence model used. However, apart from experimental conditions which are not always specified, there is also the problem of the significance of the unsteady Reynolds-averaged Navier–Stokes calculations when the massive large-scale motion has frequencies which make the concept of an instantaneous mean flow rather dubious.

APPENDIX

Some tests of grid sensitivity have been performed for both the K–ω model and the BB model. Results are given in Figure 9. Figure 10 demonstrates the good repeatability of aerodynamic coefficients between cycles 1, 2 and 3.

REFERENCES

1. W. J. Chyu, S. S. Davis and K. S. Chang, 'Calculation of unsteady transonic flow over an aerofoil', *AIAA J.*, **19**, 684–690 (1981); see also *AIAA Paper 79-1554*, 1979.
2. S. J. Shamroth and H. J. Gibeling, 'Navier–Stokes solution of the turbulent flow field about an isolated aerofoil', *AIAA J.*, **18**, 1409–1410 (1980); see also *AIAA Paper 79-1543*, 1979.
3. S. J. Shamroth and H. J. Gibeling, 'Analysis of turbulent flow about an isolated aerofoil using a time-dependent Navier–Stokes procedure', *AGARD GP 296*, 1980.
4. Y. Tassa and N. L. Sankar, 'Dynamic stall of NACA 0012 aerofoil in turbulent flow—numerical study', *AIAA Paper 81-1289*, 1981.
5. N. L. Sankar and Y. Tassa, 'Compressibility effects on dynamic stall of a NACA 0012 aerofoil', *AIAA J.*, **19**, 557–558 (1981); see also *AIAA Paper 80-0010*, 1980.
6. H. A. Hegna, 'Numerical prediction of dynamic forces on arbitrarily pitched aerofoils', *AIAA J.*, **21**, 161–162 (1983); see also *AIAA Paper 82-0092*, 1982.
7. C. L. Rumsey and W. K. Anderson, 'Some numerical and physical aspects of unsteady Navier–Stokes computations over aerofoils using dynamic meshes', *AIAA Paper 88-0329*, 1988.
8. M. R. Visbal, 'Evaluation of an implicit Navier–Stokes solver for some unsteady separated flows', *AIAA Paper 86-1053*, 1986.
9. M. R. Visbal, 'Effect of compressibility on dynamic stall of a pitching aerofoil', *AIAA Paper 88-0132*, 1988.
10. M. R. Visbal, 'Dynamic stall of a constant-rate pitching aerofoil', *AIAA Paper 91-0006*, 1991.
11. I. H. Tuncer, J. C. Wu and C. M. Wang, 'Theoretical and numerical studies of oscillating aerofoils', *AIAA Paper 89–0021*, 1989.
12. J. Wu, D. Huff and L. N. Sankar, 'Evaluation of three turbulence models in static air loads and dynamic stall predictions', *J. Aircraft*, **27**, 382–384 (1990); see also *AIAA Paper 89-0609*, 1989.
13. M. Dindar and U. Kaynak, 'Effect of turbulence modelling on dynamic stall of a NACA 0012 aerofoil', *AIAA Paper 92-0020*, 1992.
14. D. P. Rizzetta and M. R. Visbal, 'Comparative numerical study of two turbulence models for aerofoil static and dynamic stall', *AIAA J.*, **31**, 784–786 (1993).
15. G. R. Srinivasan, J. A. Ekaterinaris and W. J. McCroskey, 'Dynamic stall of an oscillating wing, Part 1/Evaluation of turbulent models', *AIAA Paper 93-3403*, 1993.
16. J. A. Ekaterinaris, 'Compressible studies of dynamic stall', *AIAA Paper 89–0024*, 1989.
17. J. A. Ekaterinaris and F. Menter, 'Computation of oscillating aerofoil flows with one- and two-equation turbulence models', *AIAA J.*, **32**, 2359–2365 (1994); see also *AIAA Paper 94-0490*, 1994.
18. H. Q. Yang, 'Numerical simulation of dynamic stall at high Reynolds numbers', *AIAA Paper 94-0286*, 1994.
19. Y. Y. Niu, J. N. Scott and G. M. Gregorek, 'A modified flux vector split algorithm for oscillating aerofoil flow simulations', *AIAA Paper 94-0308*, 1994.

20. G. B. Deng, J. Piquet, P. Queutey and M. Visonneau, 'Navier–Stokes equations for incompressible flows: finite-difference and finite-volume methods', in R. Peyret (ed.), *Handbook of Computational Fluid Dynamics*, Academic, New York, 1996, Chap. 2, pp. 25–97.
21. F. Grasso and C. Meola, 'Euler and Navier–Stokes equations for compressible flows: finite volume methods', in R. Peyret (ed.), *Handbook of Computational Fluid Dynamics*, Academic, New York, 1996, Chap. 2, pp. 159–282.
22. B. S. Baldwin and H. Lomax, 'Thin-layer approximation and algebraic model for separated turbulent flows', *AIAA Paper 78-0257*, 1978.
23. B. S. Baldwin and T. A. Barth, 'One-equation turbulence transport model for high Reynolds number wall-bounded flows', *AIAA Paper 91- 0610*, 1991.
24. W. J. McCroskey, K. W. McAlister, L. W. Carr, S. L. Pucci, O. Lambert and R. F. Indergrand, 'Dynamic stall of advanced aerofoil sections', *J. Am. Helicopter Soc.*, 40–50 (1981).
25. W. J. McCroskey, 'The phenomenon of dynamic stall', *NASA TM 81264*, 1981.
26. W. J. McCroskey, L. W. Carr and K. W. McAlister, 'Dynamic experiments on oscillating aerofoils', *AIAA J.*, **14**, 57–63 (1976).
27. K. W. McAlister, W. J. Pucci, W. J. McCroskey and L. W. Carr, 'An experimental study of dynamic stall on advanced aerofoil sections. Pressure and force data', *NASA TM 84245*, 1982.
28. F. Menter, 'Zonal two-equations K–ω models for aerodynamic flows', *AIAA Paper 93-2906*, 1993.
29. C. M. Rhie and W. L. Chow, 'A numerical study of the turbulent flow past an isolated aerofoil with trailing edge separation', *AIAA J.*, **17**, 1525–1532 (1983); see also *AIAA Paper 82-0998*, 1982.
30. G. E. Schneider and M. J. Raw, 'Control volume finite-element method for heat transfer and fluid flow using collocated variables. 1. Computational procedure', *Numer. Heat Transfer*, **11**, 363–390 (1987).
31. G. B. Deng, J. Piquet, P. Queutey and M. Visonneau, 'Incompressible flow calculations with a consistent physical interpolation finite volume approach', *Comput. Fluids*, **23**, 1029–1047 (1994).
32. G. B. Deng, J. Piquet, P. Queutey and M. Visonneau, 'A new fully- coupled solution of the Navier–Stokes equations', *Int. j. numer. methods fluids*, **19**, 605–640 (1994).
33. G. B. Deng, E. Guilmineau, J. Piquet, P. Queutey and M. Visonneau, 'Computation of unsteady laminar viscous flow past an aerofoil using the CPI method', *Int. j. numer. methods fluids*, **19**, 765–795 (1994).
34. R. I. Issa, 'Solution of the implicitly discretized fluid flow equations by operator-splitting', *J. Comput. Phys.*, **62**, 40– 65 (1985).
35. M. Raffel, J. Kompenhans and P. Wernert, 'Investigation of the unsteady flow velocity field above an aerofoil pitching under deep dynamic stall conditions', *Exp. Fluids*, **19**, 103–111 (1995).
36. L. W. Carr, K. W. McAlister and W. J. McCroskey, 'Analysis of the development of dynamic stall based on oscillating aerofoil experiments', *NASA TN D-8382*, 1977.
37. J. Panda and K. B. M. Q. Zaman, 'Experimental investigation of the flow field of an oscillating aerofoil and estimation of lift from wake surveys', *J. Fluid Mech.*, **265**, 65–95 (1994).
38. J. De Ruick, B. Hazarika and C. Hirsch, 'Measurements of velocity profiles and Reynolds stresses on an oscillating aerofoil', *AGARD CP 468*, 1989, Paper 79.
39. M. C. Robinson, H. E. Helin and M. W. Luttges, 'Control of wake structure behind an aerofoil', *AIAA Paper 86-2282*, 1986.
40. J. G. Leishman, 'Dynamic stall experiments on the NACA 0012 aerofoil', *Exp. Fluids*, **9**, 49–58 (1990).